

The VIMOS Public Extragalactic Redshift Survey (VIPERS) [★]

A precise measurement of the galaxy stellar mass function and the abundance of massive galaxies at redshifts $0.5 < z < 1.3$

I. Davidzon^{1,2}, M. Bolzonella¹, J. Coupon³, O. Ilbert⁴, S. Arnouts^{5,4}, S. de la Torre⁶, A. Fritz⁷, G. De Lucia⁸, A. Iovino⁹, B. R. Granett⁹, G. Zamorani¹, L. Guzzo^{9,10}, U. Abbas¹¹, C. Adami⁴, J. Bel¹², D. Bottini⁷, E. Branchini^{13,14,15}, A. Cappi^{1,16}, O. Cucciati¹, P. Franzetti⁷, M. Fumana⁷, B. Garilli^{7,4}, J. Krywult¹⁷, V. Le Brun⁴, O. Le Fèvre⁴, D. Maccagni⁷, K. Małek¹⁸, F. Marulli^{2,19,1}, H. J. McCracken²⁰, L. Paoro⁷, J. A. Peacock⁶, M. Polletta⁷, A. Pollo^{21,22}, H. Schlagenhauser^{23,24}, M. Scodeggio⁷, L. A. M. Tasca⁴, R. Tojeiro²⁵, D. Vergani²⁶, A. Zanichelli²⁷, A. Burden²⁵, C. Di Porto¹, A. Marchetti^{28,9}, C. Marinoni^{12,29}, Y. Mellier²⁰, L. Moscardini^{2,19,1}, T. Moutard⁴, R. C. Nichol²⁵, W. J. Percival²⁵, S. Phleps²⁴, and M. Wolk²⁰

(Affiliations can be found after the references)

March 18, 2013

ABSTRACT

We measure the evolution of the galaxy stellar mass function from $z = 1.3$ to $z = 0.5$ using the first 53 608 redshifts of the ongoing VIMOS Public Extragalactic Survey (VIPERS). Thanks to its large volume and depth, VIPERS provides a detailed picture of the galaxy distribution at $z \approx 0.8$, when the Universe was ≈ 7 Gyr old. We carefully estimate the uncertainties and systematic effects associated with the SED fitting procedure used to derive galaxy stellar masses. We estimate the galaxy stellar mass function at several epochs between $z = 0.5$ and 1.3 , discussing in detail the amount of cosmic variance affecting our estimate. We find that Poisson noise and cosmic variance of the galaxy mass function in the VIPERS survey are comparable with the statistical uncertainties of large surveys in the local universe. VIPERS data allow us to determine with unprecedented accuracy the high-mass tail of the galaxy stellar mass function, which includes a significant number of galaxies that are usually too rare to detect with any of the past spectroscopic surveys. At the epochs sampled by VIPERS, massive galaxies had already assembled most of their stellar mass. We compare our results with both previous observations and theoretical models. We apply a photometric classification in the $(U - V)$ rest-frame colour to compute the mass function of blue and red galaxies, and we find evidence for the evolution of their contribution to the total number density budget: the transition mass above which red galaxies dominate is found to be about $10^{10.4} M_{\odot}$ at $z \approx 0.55$ and evolves proportional to $(1+z)^3$. We are able to trace separately the evolution of the number density of blue and red galaxies with masses above $10^{11.4} M_{\odot}$, in a mass range barely studied in previous work due to the small volumes surveyed. We find that for such large masses, red galaxies show a milder evolution with redshift, when compared to objects at lower masses. At the same time, we detect a population of similarly massive blue galaxies, which are no longer detectable below $z = 0.7$. These results show the improved statistical power of VIPERS data, and give initial promising indications of mass-dependent quenching of galaxies at $z \approx 1$.

Key words. Galaxies: fundamental parameters, mass function, evolution, statistics – Cosmology: observations

1. Introduction

The last decade has seen many significant advances in the study of galaxy evolution prompted by large astronomical surveys. In particular, such surveys sample large cosmic volumes collecting

large amounts of data, thus facilitating a number of important statistical studies. The galaxy stellar mass function (GSMF), defined as the co-moving number density of galaxies within a stellar mass bin $(M, M + dM)$, is one such fundamental statistic, allowing us to trace the history of baryonic mass assembly. Measurements of the GSMF help constraining the cosmic star formation rate (SFR, e.g. Behroozi et al. 2013) and investigating how galaxy properties change as a function of stellar mass, redshift, and environments (e.g. in galaxy clusters, Vulcani et al. 2011).

In the nearby universe, the GSMF has been measured to high accuracy by exploiting the Two Micron All Sky Survey (2MASS), the 2dF Galaxy Redshift Survey (2dFGRS, Cole et al. 2001), and the Sloan Digital Sky Survey (SDSS, e.g. York et al. 2000). Its shape is well parametrised by a double Schechter (1976) function, with an upturn at $M \approx 10^{10} M_{\odot}$ (Baldry et al. 2008; Li & White 2009; Baldry et al. 2012). Such bimodality, also visible in the SDSS luminosity function (Blanton et al.

Send offprint requests to: Iary Davidzon
e-mail: iary.davidzon@unibo.it

[★] Based on observations collected at the European Southern Observatory, Cerro Paranal, Chile, using the Very Large Telescope under programs 182.A-0886 and partly 070.A-9007. Also based on observations obtained with MegaPrime/MegaCam, a joint project of CFHT and CEA/DAPNIA, at the Canada-France-Hawaii Telescope (CFHT), which is operated by the National Research Council (NRC) of Canada, the Institut National des Sciences de l'Univers of the Centre National de la Recherche Scientifique (CNRS) of France, and the University of Hawaii. This work is based in part on data products produced at TERAPIX and the Canadian Astronomy Data Centre as part of the Canada-France-Hawaii Telescope Legacy Survey, a collaborative project of NRC and CNRS.

2005), is thought to be related to the existence of two distinct galaxy types: a population of star-forming galaxies, with blue colours and disc-dominated or irregular morphology, and a class of red early-type galaxies that, on the contrary, have their star formation substantially shut off (Kauffmann et al. 2003a; Franx et al. 2008; Bell et al. 2007).

At higher redshift, such studies are more challenging because of the faintness of the objects. However, early seminal work took advantage of the Hubble Space Telescope to construct samples of a few hundreds galaxies up to $z \simeq 3$, finding evidence for an increase of the average stellar mass density with cosmic time (Rudnick et al. 2003; Dickinson et al. 2003; Fontana et al. 2003). Later, deeper surveys were able to show the lack of evolution in the high-mass end of the GSMF (GOODS-MUSIC catalogue, Fontana et al. 2006) opposed to an increase of galaxy density at lower masses (VVDS survey, Pozzetti et al. 2007), a result consolidated up to $z \simeq 4$ by means of near- and mid-infrared data which facilitate better estimates of the stellar masses (Pérez-González et al. 2008; Kajisawa et al. 2009). Although some disagreements exist, such findings indicate that massive galaxies were assembled earlier than those with lower stellar mass, suggesting a ‘downsizing in stellar mass’ has taken place (Fontanot et al. 2009).

Besides these results, first attempts to study the GSMF by dividing blue/active from red/quiescent objects provided interesting results, despite the relatively limited statistics, and revealed that within the GSMF the number of blue galaxies at intermediate masses decreases as a function of cosmic time, while the fraction of red galaxies increases (Bundy et al. 2006; Borch et al. 2006). This early work was extended using larger galaxy samples (as in COSMOS and zCOSMOS, Drory et al. 2009; Ilbert et al. 2010; Pozzetti et al. 2010), or very deep observations (GOODS-NICMOS survey, Mortlock et al. 2011), producing robust results for the evolution in number density of both these galaxy populations. They also showed that a double Schechter function is a good fit to the GSMF data out to $z \simeq 1$ (Pozzetti et al. 2010; Peng et al. 2010).

A fundamental picture emerging from these studies is the transformation of star-forming galaxies into “red and dead” objects through some quenching mechanism that halts the production of new stars. To discriminate between the various quenching mechanisms proposed in the literature (see Gabor et al. 2010, and reference therein), it is crucial to obtain precise and accurate measurements to constrain theoretical models (Lu et al. 2012; Mutch et al. 2013; Wang et al. 2013). Unfortunately, such comparisons are hard, as on one side the modelling of galaxy evolution, based on N -body dark matter simulations (e.g. De Lucia & Blaizot 2007; Bower et al. 2006; Guo et al. 2011, 2013), requires a high level of complexity to parametrise all the physical processes (star formation, supernova ejecta, etc.). On the observational side, instead, it is hard to derive physical galaxy properties with sufficient precision to constrain models, especially for rare populations like the most massive galaxies (Marchesini et al. 2009, 2010).

The latest galaxy surveys are helping with accurate measurements of the GSMF, especially in the high-mass end, and could solve discrepancies between data and models (BOSS, Maraston et al. 2012). State-of-the-art analyses provide new evidence confirming the dependence on stellar mass of the physical processes that extinguish star formation: from $z = 1$ to $z = 3$, quenching is more efficient for $M \gtrsim 10^{10.8} M_{\odot}$ (Ilbert et al. 2013, using UltraVISTA data), while at $z < 1$ the number density of quiescent galaxies evolves significantly at lower masses (Ilbert et al. 2010; Moustakas et al. 2013 using PRIMUS data). The role en-

vironment plays in quenching galaxies is still debated (Cucciati et al. 2010; Iovino et al. 2010; Bolzonella et al. 2010; Peng et al. 2010; Vulcani et al. 2013).

Within this context, the VIMOS Public Extragalactic Redshift Survey (VIPERS) provides a novel opportunity. As we shall describe here, this survey provides a combination of wide angle coverage, depth and sampling that proves to be ideal to measure the GSMF at $z \sim 1$ with unprecedented precision. The large volume allows to effectively probe the massive end of the GSMF at these redshifts; compared to photometric redshift surveys, the accurate spectroscopic redshift measurements are also crucial to for an accurate measurement at the high-mass end, where a few interlopers can dramatically change the shape of the GSMF.

In this paper we present the first measurements of the GSMF from the catalogue of the first $\sim 55\,000$ objects; in this first analysis we shall concentrate on discussing the evolution of the GSMF from $z = 1.3$ down to $z = 0.5$, i.e. within the range covered by the VIPERS data, for the whole galaxy sample and separately for the blue and red populations. We shall also discuss in detail the sources of error and potential systematic effects, which become dominant at the level of precision on the GSMF allowed by the VIPERS data. These are particularly crucial when comparison with independent data is performed.

In Sect. 2 we present the the VIPERS galaxy catalogue, which has been used in this work, and describe how stellar masses have been estimated through the SED fitting technique. The global mass function is presented in Sect. 3, along with a discussion on the sample completeness and the main sources of uncertainties. We compare those results with both previous surveys and models in Sect. 4. In Sect. 5, after applying a colour classification, we study the mass function (and the related number density) of red and blue galaxies. Our results are summarised in Sect. 6. Unless specified otherwise, our cosmological framework assumes $\Omega_m = 0.25$, $\Omega_{\Lambda} = 0.75$, and $h_{70} = H_0/(70 \text{ km s}^{-1} \text{ Mpc}^{-1})$. All the magnitudes are in the AB system (Oke 1974).

2. Data

VIPERS¹ is an ongoing redshift survey aiming at observing approximately 100 000 galaxies and AGNs at intermediate redshifts ($\langle z \rangle \sim 0.8$) in the magnitude range of $17.5 \leq i \leq 22.5$. At the completion of the survey, expected in 2014, approximately 24 deg^2 will have been covered within two fields of the Canada-France-Hawaii Telescope Legacy Survey Wide (CFHTLS-Wide)², namely W1 and W4. The sky region covered at present is $\sim 7.5 \text{ deg}^2$ in each of W1 and W4, with an effective area of 5.34 deg^2 and 4.97 deg^2 respectively after accounting for the photometric and spectroscopic masks, or $\sim 10 \text{ deg}^2$ as a whole. Once completed, VIPERS will be the largest spectroscopic survey at such redshifts in terms of volume explored ($1.5 \times 10^8 \text{ Mpc}^3 h_{70}^{-3}$). All details on the survey design and construction can be found in Guzzo et al. (2013).

The main science drivers of VIPERS are the accurate measurement of galaxy clustering, bias parameter, and the growth rate of structures, along with the study of the statistical properties of galaxies and their evolution when the Universe was about half its current age. These topics are the subject of the parallel accompanying papers of this series (Guzzo et al. 2013; de la Torre et al. 2013; Marulli et al. 2013; Fritz et al. 2013; Malek

¹ <http://vipers.inaf.it>

² <http://www.cfht.hawaii.edu/Science/CFHTLS/>

et al. 2013; Bel et al. 2013). A previous smaller VIPERS sample has already been used in Granett et al. (2012) and Marchetti et al. (2013).

The spectroscopic survey is complemented by a set of photometric ancillary data, obtained from public surveys and dedicated observations, allowing us to estimate with high precision several galaxy properties, in particular galaxy stellar masses and rest-frame magnitudes.

2.1. Photometry

The VIPERS spectroscopic sample has been selected from the W1 and W4 fields of the CFHTLS-Wide. Therefore, for each galaxy we have a photometric dataset consisting of u^* , g' , r' , i' , and z' magnitudes (SEXTRACTOR's MAG_AUTO derived in double image mode in order to maintain the same aperture in all bands, Bertin & Arnouts 1996), as measured by the Terapix team for the T0005 data release (Mellier et al. 2008). The Terapix photometric masks, which discard areas around bright stars or with problematic observations, have been revisited by our team to recover regions where the photometric quality is deemed sufficient for our analysis (Guzzo et al. 2013).

We took advantage of the full wavelength range of the VIPERS photometric dataset, as this significantly improves the results of our SED fitting; in particular, near-infrared (NIR) fluxes are critical to constrain physical parameters and break degeneracies between the mean age of the stellar population and dust attenuation, and they allow to compute robust estimate of stellar masses (e.g. Lee et al. 2009).

In order to exploit the full potential of VIPERS in analysing the galaxy properties as a function of time and environment, we have undertaken a follow-up in the K -band in the two VIPERS fields with the WIRCAM instrument at CFHT and in the far- and near-UV (FUV and NUV) channel with the GALEX satellite (Arnouts et al., in prep.). The K -band observations were collected in between 2010 and 2012 with several PI and discretionary time programs. The K -band depth has been optimised to match the brightness of the spectroscopic sources: at the magnitude limit ($K_{WIRCAM} \simeq 22.0$ at 5σ), 96% of the spectroscopic sample in W4 is observed in K_{WIRCAM} , while in W1 this percentage is approximately 80%.

In addition to WIRCAM data, we match our CFHTLS optical catalogue with the recent UKIDSS data releases³ using a matching radius of $0.8''$. The W1 field overlaps with UDS and DXS, whereas the W4 field is fully covered by the shallower LAS and partially covered by DXS. We use, where available, Petrosian magnitudes in the Y , J , H and K bands converted in the AB system. Considering also K_{UKIDSS} , the percentage of our spectroscopic sample with K -band magnitude increases to 97% in W1 and 95% in W4.

We compare the K -band photometry for optical sources matched with both UKIDSS and WIRCAM surveys, and find a good agreement. In fact, we find a mean difference $\langle \Delta K \rangle = \langle K_{WIRCAM} - K_{UKIDSS} \rangle \simeq -0.05$, with a small dispersion $\sigma_{\Delta K} \simeq 0.10$ and 0.15 , for W1 and W4 respectively. These differences can be ascribed to the transmission functions of the filters and the definition of the aperture used when measuring magnitudes, and are of the order of photometric errors. To not overweight the K -band magnitudes in the SED fitting, only the deeper K_{WIRCAM} has been used when both magnitudes were available for the same object.

Besides the NIR magnitudes, the UV part of the spectrum can also be important for constraining the galaxy dust content and the star formation rate. We make use of existing GALEX images observed with the deep imaging survey (integration time $\sim 3 \times 10^4$ s) in NUV and FUV channel and we have completed the coverage in W1 region with new observations in NUV channel only and with integration time $T_{exp} > 1.5 \times 10^4$ s. Because of the GALEX large PSF (~ 5 arcsec), the source blending is a major issue in GALEX deep imaging mode. To measure the UV fluxes of the sources, we use the dedicated photometric algorithm EMphot (Conseil et al. 2011) which adopts the positions of U band selected priors and performs a modelled PSF adjustment over small tiles based on the expectation maximisation algorithm (Guillaume et al. 2006). For our spectroscopic sample, 63% (15%) of the sources have a NUV (FUV) flux measurements in W1. In contrast, the W4 field has a modest GALEX coverage with 13% (5%) of spectroscopic sources with a NUV (FUV) flux. The WIRCAM and GALEX datasets in the VIPERS fields are described in Arnouts et al. (in prep.).

Moreover, for $\sim 30\%$ of the spectroscopic targets already observed in W1, we also took advantage of the SWIRE observations in the XMM-LSS field. During the SED fitting we only considered magnitudes in the $3.6\mu m$ and $4.5\mu m$ bands, since at longer wavelengths the source detection is very sparse. Moreover, at those wavelengths the re-emission from the dust begins to contribute to the flux of galaxies, and this feature is not reproduced by most of the models of stellar population synthesis (see Sect. 2.3).

2.2. Spectroscopy

The spectroscopic catalogue used in this paper represents the first 60% of VIPERS. This sample includes 53608 galaxy spectra and will be made available through the future VIPERS Public Data Release 1 (PDR-1). The VIPERS targets were selected via two criteria. The first was aimed at separating galaxies and stars, and relies on the combination of a point-like classification (based on the measure of the half-light radius) for the brightest sources, and on the comparison of the five optical magnitudes with galaxy and stellar spectral energy distributions for the faintest ones (Coupon et al. 2009). A fraction of the point-like sources are targeted as AGN candidates, when located in the AGN loci of the two colour diagrams ($g - r$) versus $(u - g)$ and $(g - i)$ versus $(u - g)$. The second selection criterion, based on $(g - r)$ and $(r - i)$ colours, has been developed to exclude low redshift ($z < 0.5$) objects, and has been tested to ensure it does not introduce any significant bias. A complete description of the whole source selection procedure is included in Guzzo et al. (2013).

The spectroscopic observations have been carried out using the VIMOS instrument on VLT LR-Red grism ($R = 210$), giving a wavelength range of $5500\text{--}9500\text{ \AA}$ that guarantees the observability of the main spectral features in the VIPERS redshift range, e.g. the absorption lines CaII H & K $\lambda\lambda 3934, 3969$ and the emission line [OII] $\lambda 3727$. Using a sample of objects spectroscopically observed twice, we are able to estimate an uncertainty of $\sigma_z = 0.00047(1+z)$ for our measured redshifts.

To maximise the multiplex capability of VIMOS, we adopt the observational strategy described in Scodeggio et al. (2009) of using shorter slits than in the previous surveys carried out with the same instrument. By virtue of this strategy, we reached a sampling rate of approximately 40% with a single pass, essential

³ DR9 for LAS and DXS, DR8 for UDS; <http://www.ukidss.org/>

to estimate the large scale environment (Cucciati et al., in prep.; Iovino et al., in prep).

The spectroscopic masks reproduce the footprint of the VIMOS instrument, consisting of 4 quadrants and gaps between them for each pointing, covering 224 arcmin^2 . Moreover, vignetted parts of the quadrants have been removed to compute the effective area (for a detailed description see Guzzo et al. 2013).

Data reduction and redshift measurement have been performed within the software environment EasyLife (Garilli et al. 2012), based on the VIPGI pipeline (Scodeggio et al. 2005) and EZ (Garilli et al. 2010, Easy redshift). Spectroscopic redshifts have been determined independently by two team members and reconciled in case of discordance. Each redshift has a confidence assigned by using a well-established scheme developed by previous surveys like VVDS (Le Fèvre et al. 2005) and zCOSMOS (Lilly et al. 2009). In detail, a spectroscopic quality flag of 4 corresponds to a confidence level of 99.6% (Guzzo et al. 2013), down to a confidence level of 0, which represents the lack of a reliable redshift estimate. Moreover, objects with a single emission line are labelled by flag 9, and broad-line AGNs share the same scheme, but their flags are increased by 10. Each spectroscopic flag also has a decimal digit specifying the agreement with the photometric redshift computed from CFHTLS photometry (Coupon et al. 2009).

After excluding galaxies without redshifts (flag 0) and stars, our redshift sample contains 53 608 extragalactic sources, nearly equally split between the two fields. The quality of redshift measurements for the sample with spectroscopic flags larger than 2, as estimated from the validation of multiple observations, is high (confidence > 95%, see Guzzo et al. 2013).

Since a fraction of all the possible targets have been observed, statistical weights are required to make this subsample representative of all the galaxies at $i \leq 22.5$ in the survey volume. Such weights are calculated taking into account the number of photometric objects that have been targeted (target sampling rate, TSR), the fraction of them classified as secure measurements (spectroscopic success rate, SSR), and the completeness due to the colour selection (colour sampling rate, CSR; for a detailed discussion see Guzzo et al. 2013; Fritz et al. 2013). The statistical weights can depend on the magnitude, redshift, colour, and angular position of the considered object. For each part of the statistical weight we considered only the main and relevant dependencies, in order to avoid spurious fluctuations in case of small subsamples.

In particular, we considered the TSR as a function only of the selection magnitude, the SSR as a function of magnitude and redshift, and the CSR (estimated by using data from the VVDS flux limited survey, Le Fèvre et al. 2005) as a function of redshift. Regarding the SSR, only galaxies with quality flag between 2 and 9 ($\sim 41\,100$ galaxies in the redshift range $0.5 \leq z \leq 1.3$) have been considered in the analysis (we exclude spectra classified as broad-line AGNs). For a galaxy at redshift z with magnitude i , its statistical weight $w(i, z)$ is the inverse of the product of $\text{TSR}(i)$, $\text{SSR}(i, z)$, and $\text{CSR}(z)$. Once each galaxy in the spectroscopic sample is properly weighted, we can recover the properties of the photometric parent sample with good precision (see Fritz et al. 2013, for the details on TSR, SSR, and CSR).

2.3. Stellar masses

Considering the small fraction of objects without K band magnitude, we decided to rely on SED fitting to derive stellar masses and to not implement alternative methods such as the Lin et al.

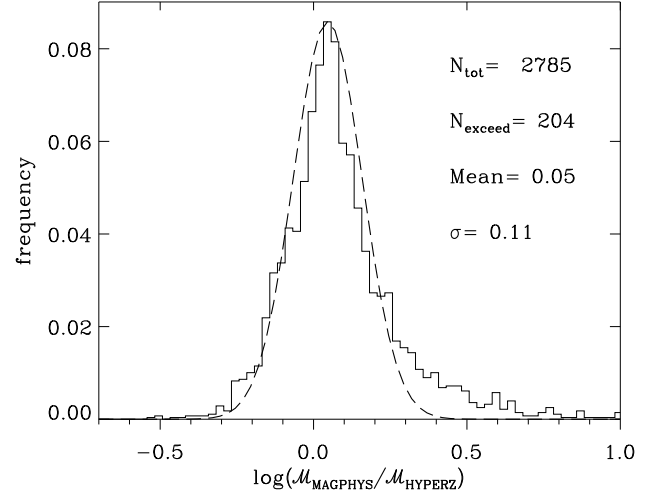


Fig. 1. Distribution of the differences between the values of stellar mass estimated using the two codes *Hyperzmass* and *MAGPHYS*. Only results on the W1 field are shown (see text). To limit the effects of parameter degeneracy, we restrict the comparison to galaxies that turn out to have solar metallicity, according to their best-fit SED both in *Hyperzmass* and *MAGPHYS*. In this way $\log(M_{\text{MAGPHYS}}/M_{\text{Hyperzmass}})$ cannot be due to a different metal content assumed in the two SED fitting estimates. The red dashed line gives the best-fitting Gaussian of the distribution, corresponding to the mean and standard deviation indicated. Also indicated are the size of the galaxy subsample (N_{tot}) and the number of stellar mass estimates for which the discrepancy is $\log(M_{\text{MAGPHYS}}/M_{\text{Hyperzmass}}) > 2\sigma$ (N_{exceed}).

(2007) relation between stellar mass, redshift and rest-frame magnitudes.

We thus derive galaxy stellar masses (M) by means of an updated version of *Hyperzmass* (Bolzonella et al. 2000, 2010, the software is available on request). Given a set of synthetic spectral energy distributions, the software fits these models to the multi-band photometry for each galaxy and selects the model that minimises the χ^2 . The SED templates involved in this procedure are derived from simple stellar populations (SSP) modelled by Bruzual & Charlot (Bruzual & Charlot 2003, hereafter BC03), adopting the Chabrier (2003) universal initial mass function (IMF)⁴. The BC03 model is one of the most used in literature (e.g. Ilbert et al. 2010; Zahid et al. 2011; Barro et al. 2013). Another commonly used SSP library is the one by Maraston (M05, 2005), which differs from the former because of the treatment of the thermally pulsing asymptotic giant branch (TP-AGB) stellar phase, especially affecting NIR emission of stellar populations aged ~ 1 Gyr. The issue about the TP-AGB role in the stellar population synthesis is still open (e.g. Marigo & Girardi 2007), with some evidences that supports BC03 (Kriek et al. 2010; Zibetti et al. 2013) in contrast with observations favouring M05 (MacArthur et al. 2010). In the following we prefer to adopt the BC03 model, since most of the galaxies in the redshift range we explored should not be dominated by the TP-AGB phase (which is instead relevant for galaxies at $1.4 \leq z \leq 2.7$ Maraston et al. 2006).

⁴ The choice of a different IMF turns into a systematic mean offset in the stellar mass distribution: for instance, our estimates can be converted to a Salpeter (1955) IMF by a scaling factor of ~ 1.7 , and ~ 1.1 for switching to Kroupa (2001).

The SSPs provided by [Bruzual & Charlot \(2003\)](#) assume a non-evolving stellar metallicity Z , which we chose to be solar ($Z = Z_{\odot}$) or sub-solar ($Z = 0.2Z_{\odot}$). This choice allows us to take into account the different metallicities of the galaxies in our redshift range, which can be lower than in the nearby universe ([Zahid et al. 2011](#)), without significantly increasing the effect of the age-metallicity degeneracy. Considering the low resolution of our spectroscopic setup, it is difficult to put reliable constraints on Z from the observed spectral features, and therefore it was not possible to constrain this parameter *a priori*. Therefore, the metallicity assigned to each galaxy is that obtained from the best-fit model (smallest χ^2).

With respect to the galaxy dust content, we implement the [Calzetti et al. \(2000\)](#) and [Prévot-Bouchet \(Prevot et al. 1984; Bouchet et al. 1985\)](#) extinction model, with values of A_V ranging from 0 (no dust) to 3 magnitudes. As pointed out by [Ilbert et al. \(2009\)](#), Calzetti's law is on average more suitable for the bluest SEDs, having been calibrated on starburst (SB) galaxies, whereas the [Prévot-Bouchet](#) law is better for mild star-forming galaxies, as it was derived from the dust attenuation of the Small Magellanic Cloud (SMC) (see also [Wuyts et al. 2011](#)). Hereafter we refer to the Calzetti and [Prévot-Bouchet](#) models as SB and SMC extinction laws respectively. We let the choice between the two extinction laws free, according to the best fit model (smallest χ^2), since we do not have sufficient data at UV wavelengths to discriminate between the different trends of the two laws.

The SEDs constituting our template library are then generated from the SSPs following the evolution described by a given star formation history (SFH). In this work, we assume exponentially declining SFHs, for which $\text{SFR} \propto \exp(-t/\tau)$, with the time scale τ ranging from 0.1 to 30 Gyr. A constant SFH (i.e., $\text{SFR} \sim 1 M_{\odot} \text{yr}^{-1}$) is also considered.

Although such a parametrisation is widely used, recent studies have shown how exponentially increasing SFHs can provide a more realistic model for actively star-forming galaxies in which young stellar populations out-shine the older ones ([Maraston et al. 2010](#)). This effect becomes relevant at $z \sim 2$, when the cosmic star-formation peaks, and can be reduced by setting a lower limit on the age parameter, in order to avoid unrealistic solutions that are too young and too dusty ([Pforr et al. 2012](#)). In our redshift range, galaxies whose SFH rises progressively have small stellar masses ($\log(M/M_{\odot}) \sim 9.5$, [Pacifci et al. 2013](#)) falling below the limit of VIPERS.

Moreover, [Pacifci et al. \(2013\)](#) identify a class of massive blue galaxies that assembled their stellar mass over a relatively long period, experiencing at a later stage the progressive reduction of their star formation. For such *bell-shaped* SFH, neither increasing nor decreasing τ -models seem to be suitable. However, the resulting differences are smaller than the other uncertainties of the SED fitting method (cf. [Conroy et al. 2009](#)), and the stellar masses computed assuming τ -models are adequate for our analysis.

Another issue concerning the SFH is the assumption of its smoothness. In fact, a real galaxy could have experienced several phases of intense star-formation during its past, which can be taken into account by superimposing random peaks on the exponential (or constant) SFR ([Kauffmann et al. 2003a](#)). Allowing the presence of recent secondary bursts, making the colours of an underlying older and redder population bluer, can lead to a systematically larger stellar mass estimate, but only for a small fraction of objects the difference in M is larger than 0.2 dex, as shown by [Pozzetti et al. \(2007\)](#).

We also quantified the effect of complex SFHs in VIPERS, by computing stellar masses using the *MAGPHYS* package ([da](#)

[Cunha et al. 2008](#)). This code parametrises the star formation activity of each galaxy template starting from the same SSP models as *Hyperzmass* (i.e. BC03), but using two components in the SFH, namely an exponentially declining SFR and a second component of additional bursts randomly superimposed to the former according to [Kauffmann et al. \(2003a\)](#). The probability of a secondary burst to occurring is such that half of the galaxy templates in the library have experienced a burst in their last 2 Gyr. Each of those episodes can last 3×10^7 – 3×10^8 yr, producing stars at a constant rate. The ratio between the stellar mass produced in a single burst and that formed over the entire galaxy life by the underlying exponentially declining model is distributed logarithmically between 0.03 and 4.0. *MAGPHYS* also treats dust attenuation in a consistent way, adopting the model proposed by [Charlot & Fall \(2000\)](#), and with the re-emission at infrared wavelengths. However, this feature does not represent a significant advantage when dealing with VIPERS data as infrared magnitudes are too sparse in our catalogue. Metallicity values are distributed uniformly between 0.02 and $2Z_{\odot}$. The large range of tightly sampled metallicities, the different model for the dust extinction, and in particular the complex SFHs in the *MAGPHYS* library are the major differences to the *Hyperzmass* code.

In Fig. 1 we compare the estimates obtained through *MAGPHYS* and *Hyperzmass*, and verify that complex SFHs have a minimal impact on the results. Since *MAGPHYS* requires much longer computational time than other SED fitting codes, we only estimate the stellar mass for galaxies in the W1 field between $z = 0.5$ and $z = 1.3$. Moreover, we select objects with the same (solar) metallicity in both the SED fitting procedures. In this way we are able to investigate the bias mainly due to the different SFH parametrisations. We find a small offset ($\langle \Delta \log M \rangle = \langle \log(M_{\text{MAGPHYS}}/M_{\text{Hyperzmass}}) \rangle \simeq 0.05$) and a small dispersion ($\sigma_{\Delta M} \simeq 0.11$), with significant differences between *MAGPHYS* and *Hyperzmass* (i.e., $\Delta \log M > 0.22$) for $\sim 7\%$ of the testing sample (N_{exceed} in Fig. 1). The consequences on the GSMF are discussed in Sect. 3.4.

Given the large range of physical properties allowed in the SED fitting procedure, we decide to exclude from the fitting some unphysical parameter combinations. In particular, we limit the amount of dust in passive galaxies (i.e., we impose $A_V \leq 0.6$ for galaxies with $\text{age}/\tau > 4$), we avoided very young extremely star-forming galaxies with short τ timescales (i.e. we prevent fits with models with $\tau \leq 0.6$ Gyr when requiring $z_{\text{form}} < 1$), and we only allow ages to be within the range between 0.1 Gyr and the age of the universe at the spectroscopic redshift of the fitted galaxy (see [Pozzetti et al. 2007; Bolzonella et al. 2010](#)).

According to [Conroy et al. \(2009\)](#), the uncertainties associated with the SED fitting can be ~ 0.3 dex when considering all the possible parameters involved and their allowed ranges. In particular, given the non-uniform coverage of the GALEX and SWIRE ancillary data matched with our sample, we checked that the variation in the magnitude set from one object to another is not introducing any bias. For the subsample of galaxies with *FUV*, *NUV*, $3.6\mu\text{m}$, and $4.5\mu\text{m}$ bands available, we estimate the stellar mass also using just the optical-NIR photometry. We find no systematic difference in the two estimates of stellar mass (with and without the UV and infrared photometry) and only a small dispersion of about 0.08 dex.

In summary, the VIPERS galaxy stellar mass estimates are obtained using the BC03 population synthesis models with Chabrier IMF, smooth (exponentially declining or constant) SFHs, solar and sub-solar metallicity, and the SB and SMC laws for modelling dust extinction. Unless stated otherwise, this is the default parametrisation used throughout this paper.

3. From stellar masses to the galaxy stellar mass function

In this Section we exploit the VIPERS dataset described above, considering only our fiducial sample of 41 094 galaxies at $z = [0.5, 1.3]$ with spectroscopic redshift reliability $> 95\%$ (see Sect. 2.2). As mentioned before, broad line AGN (~ 850 in the present spectroscopic sample) are naturally excluded from the sample, being visually identified during the redshift measurement process. Instead, narrow line AGN are not removed from our sample, but they do not constitute an issue for the SED fitting derived properties, since in most of the cases their optical and NIR emission are dominated by the host galaxy (Pozzi et al. 2007). First of all we try to identify the threshold below which the sample can be considered complete, and the mass function reliable. After that, we derive the GSMF of VIPERS in various redshift bins and discuss the main sources of uncertainty affecting it.

3.1. Completeness

In the literature, the completeness mass limit of a sample at a given redshift is often defined as the highest stellar mass a galaxy could have, when its observed magnitude matches the flux limit (e.g. Pérez-González et al. 2008). In that case, the maximum of the stellar mass estimates is reached by the rescaled SED of an old passive galaxy, which gives rise to a limiting mass that is too conservative. In fact, because of the variety of mass-to-light ratios M/L characterising the different galaxy types, this boundary in stellar mass strongly depends on the observed galaxy mix. At the limiting magnitude of a survey, blue galaxies (with low M/L) are the dominant population (e.g. Zucca et al. 2006), whereas red galaxies are generally less numerous. Therefore, the M/L range of galaxies around the magnitude limit is much narrower than the same range for the total sample, and usually it does not include the large M/L values (typical of old passive galaxies) used by the authors to estimate the completeness (see the discussion in Marchesini et al. 2009, Appendix C).

Instead, we apply the technique devised by Pozzetti et al. (2010). This procedure yields, at a certain redshift and for a fixed flux limit, an estimate of the threshold M_{lim} below which some galaxy type cannot be detected any longer. Following this approach, we estimate the stellar mass each object would have if its magnitude, at the observed redshift, were equal to the i -band limiting magnitude i_{lim} . This boundary mass $M(i = i_{\text{lim}})$ is obtained by rescaling the original stellar mass of the source at its redshift, i.e. $\log M(i = i_{\text{lim}}) = \log M + 0.4(i - i_{\text{lim}})$. The threshold M_{lim} is then defined as the value above which 90% of the $M(i = i_{\text{lim}})$ distribution lies. According to this, at values larger than M_{lim} our GSMF can be considered complete. We include in the computation only the 20% faintest objects to mitigate the contribution of the small number of bright red galaxies having large M/L . In this way we improve the method mentioned at the beginning of this Section, allowing us to extend the measurement to lower masses.

Since the $1/V_{\text{max}}$ method (Schmidt 1968, see Sect. 3.2) intrinsically corrects the sample incompleteness above the lower limit of the considered redshift bin z_{inf} , we apply to each redshift bin the M_{lim} computed considering the objects inside a narrow redshift interval $\Delta z = 0.05$ centred in z_{inf} . Figure 2 shows M_{lim} as a function of redshift for the global and for the red and blue samples used in Sect. 5, as well as the value of $M(i = i_{\text{lim}})$ for each red and blue galaxy. As expected, the limiting mass in-

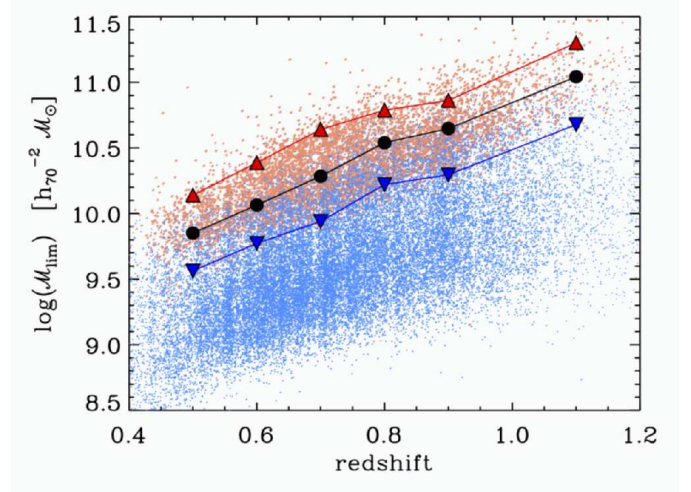


Fig. 2. The mass completeness threshold M_{lim} as a function of redshift, computed for the total sample (the one used in Sect. 3.2, filled circles) and for the red (upward triangles) and blue (downward triangles) populations, defined as discussed in Sect. 5. In each redshift bin, the M_{lim} estimate relies on the rescaled stellar mass $M(i = i_{\text{lim}})$ of the 20% faintest galaxies (see text). We show $M(i = i_{\text{lim}})$ of the red and blue galaxies with small dots of analogous colours.

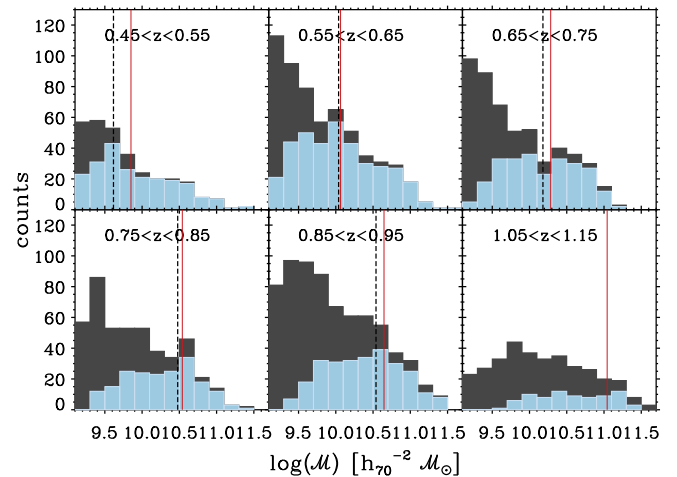


Fig. 3. Distributions of stellar masses in six redshift bins for the VVDS-Deep sample in the CFHTLS-W1 field at its limiting magnitude ($I \leq 24$, dark histograms), compared to the subset obtained by applying a VIPERS-like magnitude limit $I \leq 22.5$ (blue histograms). In each panel, the black dashed line represents the limiting mass for the latter sample, according to the method described in Sect. 3.1. The red solid line instead gives the limiting mass estimated through the same method, but for the VIPERS sample in the W1 field. Both limits correctly identify the threshold below which the shallower sample starts to miss a significant fraction ($> 20\%$) of objects.

creases as a function of z and the values for red galaxies are much larger than for the blue ones.

In the context of the zCOSMOS project (Lilly et al. 2009), the approach of Pozzetti et al. (2010) produced completeness limits in good agreement with those obtained through mock survey samples (Meneux et al. 2009). In VIPERS, we successfully tested our M_{lim} estimates taking advantage of the VVDS-Deep field, which is located in the W1 field (see Guzzo et al. 2013, Fig. 2). The VVDS sample provides us with spectroscopically observed galaxies up to a fainter limit, $I_{\text{AB}} = 24$ (Le Fèvre et al.

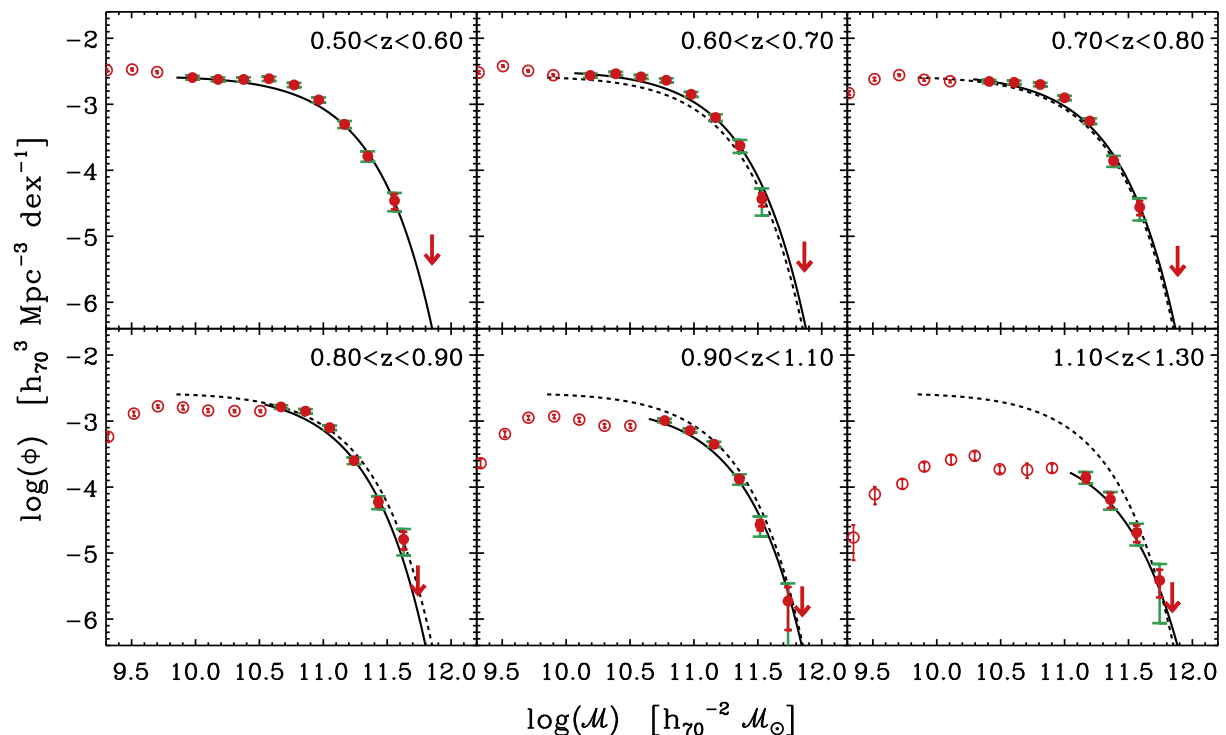


Fig. 4. The VIPERS galaxy stellar mass function at different redshifts. The circles give the values determined through $1/V_{\max}$ in mass bins of $\Delta M = 0.2$ dex; the centre of each bin corresponds to the weighted mean mass of the objects within it. Empty and filled symbols correspond to values below and above the completeness limit, respectively (see Sect. 3.1). For the latter points, the red error bars show the uncertainty due to Poisson noise, while green bars account for Poisson noise and cosmic variance. In each panel, a solid line shows the Schechter fit to the GSMF points, with the dashed line reproducing that of the first redshift bin, as a reference. The arrows give an upper limit to Φ where no detection is available.

2005). Since the CFHTLS-W1 field contains both VVDS and part of VIPERS, we can compare the stellar masses relying on a similar photometric baseline ($u, g, r, I, i, z, J^*, K^*$). When applying a VIPERS-like magnitude cut ($I < 22.5$), we can find the fraction of missed objects with respect to the parent $I < 24$ sample as a function of stellar mass. This test is shown in Fig. 3, where we compare the values of the VVDS and VIPERS M_{lim} for $I < 22.5$ to the distribution of stellar masses belonging to the deeper VVDS sample. The M_{lim} values we computed represent well the limit at which the stellar mass distribution starts to be incomplete with respect to the deep VVDS sample (i.e. the $I < 22.5$ sample recovers less than 80% of the parent sample).

3.2. Evolution of the mass function for the global population

The number of galaxies and volume sampled by VIPERS allows us to obtain an estimate of the GSMF with high statistical precision within six redshifts bins in the range $0.5 \leq z \leq 1.3$. Given the large number of galaxies observed by VIPERS, in terms of Poisson noise it would be possible to choose even narrower bins (e.g. $\Delta z \approx 0.05$ wide). However, in that case the measurements start being strongly affected by cosmic (sample) variance. A more detailed discussion is given in Sect. 3.3.

We compute the GSMF within each redshift bin, using the classical non-parametric $1/V_{\max}$ estimator (Schmidt 1968). With this method, the density of galaxies in a given stellar mass bin is obtained as the sum of the inverse of the volumes in which each galaxy would be observable, multiplied by the statistical weight described in Sect. 2.2. To optimise the binning in stellar mass,

we use an adaptive algorithm that extends the width of a bin until it contains a minimum number of objects. The errors associated with the $1/V_{\max}$ estimates are computed assuming Poisson statistics. The upper limits for non-detections have been estimated following Gehrels (1986). The values of the $1/V_{\max}$ GSMF and associated Poisson errors are given in Table 1.

It is well known that the $1/V_{\max}$ estimator is unbiased in case of a homogeneous distribution of sources (Felten 1976), but it is affected by the presence of clustering (Takeuchi et al. 2000). At variance with the data sets on which the estimator was tested in the past, VIPERS has a specific advantage, thanks to its large volume over two independent fields. The competing effects of over- and under-dense regions on the estimate should in such a situation cancel out. Moreover, as shown in Takeuchi et al. (2000), an inhomogeneous distribution of sources mainly affects the faint end (i.e. the low mass end) of the luminosity (mass) function, and the impact on our analysis will be negligible, as we are mainly interested in the massive tail of the distribution.

To verify this, we also compare the $1/V_{\max}$ estimates with those from a different software package (ALF, Ilbert et al. 2005), which includes several estimators for the luminosity and mass functions. We find no significant differences in the obtained mass functions, within the stellar mass range considered in the present study.

Finally, in addition to the non-parametric method, we fit a Schechter function (Schechter 1976) to the $1/V_{\max}$ estimates:

$$\Phi(M)dM = \Phi_* \left(\frac{M}{M_*} \right)^\alpha \exp \left(-\frac{M}{M_*} \right) \frac{dM}{M_*}. \quad (1)$$

Table 1. Global GSMF: $1/V_{\max}$ values in regular bins of stellar mass.

$\log \mathcal{M} [h_{70}^{-2} M_{\odot}]$	$\log \Phi [h_{70}^{-3} \text{Mpc}^3]$					
	$0.5 < z < 0.6$	$0.6 < z < 0.7$	$0.7 < z < 0.8$	$0.8 < z < 0.9$	$0.9 < z < 1.1$	$1.1 < z < 1.3$
9.50	$-2.47^{+0.02}_{-0.02}$	$-2.42^{+0.01}_{-0.02}$	$-2.62^{+0.02}_{-0.02}$	$-2.89^{+0.03}_{-0.03}$	$-3.20^{+0.04}_{-0.04}$	$-4.11^{+0.11}_{-0.15}$
9.70	$-2.51^{+0.02}_{-0.02}$	$-2.49^{+0.01}_{-0.01}$	$-2.56^{+0.02}_{-0.02}$	$-2.78^{+0.02}_{-0.02}$	$-2.95^{+0.03}_{-0.03}$	$-3.95^{+0.07}_{-0.08}$
9.90	$-2.61^{+0.02}_{-0.02}$	$-2.56^{+0.02}_{-0.02}$	$-2.63^{+0.02}_{-0.02}$	$-2.79^{+0.03}_{-0.03}$	$-2.93^{+0.03}_{-0.03}$	$-3.69^{+0.06}_{-0.07}$
10.10	$-2.67^{+0.02}_{-0.02}$	$-2.59^{+0.02}_{-0.02}$	$-2.65^{+0.02}_{-0.02}$	$-2.84^{+0.02}_{-0.02}$	$-2.98^{+0.03}_{-0.03}$	$-3.58^{+0.07}_{-0.08}$
10.30	$-2.68^{+0.02}_{-0.02}$	$-2.59^{+0.01}_{-0.01}$	$-2.69^{+0.02}_{-0.02}$	$-2.85^{+0.02}_{-0.02}$	$-3.07^{+0.03}_{-0.03}$	$-3.53^{+0.06}_{-0.07}$
10.50	$-2.66^{+0.02}_{-0.02}$	$-2.62^{+0.01}_{-0.01}$	$-2.70^{+0.02}_{-0.02}$	$-2.85^{+0.02}_{-0.02}$	$-3.07^{+0.03}_{-0.03}$	$-3.73^{+0.05}_{-0.05}$
10.70	$-2.72^{+0.02}_{-0.02}$	$-2.67^{+0.01}_{-0.01}$	$-2.75^{+0.01}_{-0.02}$	$-2.83^{+0.02}_{-0.02}$	$-3.04^{+0.02}_{-0.02}$	$-3.74^{+0.10}_{-0.13}$
10.90	$-2.91^{+0.02}_{-0.02}$	$-2.81^{+0.02}_{-0.02}$	$-2.83^{+0.02}_{-0.02}$	$-2.97^{+0.02}_{-0.02}$	$-3.16^{+0.02}_{-0.02}$	$-3.71^{+0.06}_{-0.07}$
11.10	$-3.25^{+0.03}_{-0.03}$	$-3.11^{+0.02}_{-0.02}$	$-3.14^{+0.02}_{-0.02}$	$-3.26^{+0.02}_{-0.03}$	$-3.32^{+0.02}_{-0.03}$	$-3.93^{+0.07}_{-0.09}$
11.30	$-3.66^{+0.05}_{-0.05}$	$-3.55^{+0.04}_{-0.04}$	$-3.59^{+0.04}_{-0.04}$	$-3.83^{+0.04}_{-0.05}$	$-3.81^{+0.04}_{-0.04}$	$-4.13^{+0.09}_{-0.12}$
11.50	$-4.34^{+0.09}_{-0.12}$	$-4.22^{+0.07}_{-0.09}$	$-4.29^{+0.07}_{-0.09}$	$-4.54^{+0.09}_{-0.12}$	$-4.39^{+0.07}_{-0.08}$	$-4.65^{+0.11}_{-0.15}$
11.70	$-5.29^{+0.23}_{-0.53}$	$-5.69^{+0.30}_{-\text{inf}}$	$-5.05^{+0.16}_{-0.26}$	$-5.19^{+0.18}_{-0.30}$	$-5.78^{+0.23}_{-0.54}$	$-5.20^{+0.14}_{-0.21}$

The results are shown in Fig. 4. The $1/V_{\max}$ determinations are marked with filled circles when they are above the completeness limit \mathcal{M}_{lim} (see Sect. 3.1). Although the mass function does not show evidence for a rapid decline below this threshold (cf. Drory et al. 2009), the open circles should be conservatively considered as lower limits. The solid lines give the best-fit using a Schechter function.

These plots show clearly the statistical power of the VIPERS sample, which includes a significant number of the rare massive galaxies that populate the GSMF high-mass end, thanks to its large volume.

At $z < 0.6$ we detect the characteristic dip of the mass function at $\log(\mathcal{M}/M_{\odot}) \sim 10.2$, with an upturn below that value as observed both locally (e.g. Baldry et al. 2012) and at intermediate redshifts (e.g. Drory et al. 2009; Pozzetti et al. 2010). However, we avoid using a double Schechter function in our fits, to ease comparison with the parameters derived at higher redshifts. In fitting the points in the first bin ($0.5 < z < 0.6$), all parameters of Eq. 1 are left free, obtaining a value of the slope $\alpha = -0.95$. Above this redshift, however, the slope of the low-mass end is only weakly constrained, given the relatively large values of the completeness limit \mathcal{M}_{lim} . For this reason, in all the other bins we fix α to the value -0.95 (see Table 2).

The results of Fig. 4 show with impressive statistical precision the lack of evolution since $z \simeq 1.1$ of the massive end ($\log(\mathcal{M}/M_{\odot}) > 11$) of the galaxy mass function seen in previous, smaller samples. The exponential tail of the Schechter fit is in fact nearly constant across the five redshift bins, down to $z \simeq 0.5$ (see Fig. 4). However, we detect a significant decrease between $z = 1.1$ and 1.3 , of the number density over the same mass range. At lower masses ($10.8 < \log(\mathcal{M}/M_{\odot}) < 11.1$) the first signs of evolution with respect to $z \sim 0.5$ start to be visible at redshift $0.9 - 1.1$.

These trends can be better evidenced in Fig. 5, where the number density of galaxies ρ_N within three mass ranges is plotted versus redshift. This figure explicitly shows that the most massive galaxies are virtually already in place at $z \simeq 1$. On the contrary, galaxies with smaller mass keep assembling their stars in such way that their number density increases by a factor ~ 3.5

Table 2. Global GSMF: Schechter parameters

z range	α	$\log \mathcal{M}_{\star}$	Φ_{\star}
		$[h_{70}^{-2} M_{\odot}]$	$[10^{-3} h_{70}^{-3} \text{Mpc}^3]$
0.5 – 0.6	$-0.95^{+0.03}_{-0.02}$	$10.87^{+0.02}_{-0.02}$	$1.42^{+0.06}_{-0.07}$
0.6 – 0.7	-0.95	$10.91^{+0.02}_{-0.01}$	$1.58^{+0.05}_{-0.05}$
0.7 – 0.8	-0.95	$10.91^{+0.01}_{-0.02}$	$1.38^{+0.06}_{-0.04}$
0.8 – 0.9	-0.95	$10.85^{+0.02}_{-0.02}$	$1.29^{+0.09}_{-0.09}$
0.9 – 1.1	-0.95	$10.91^{+0.02}_{-0.01}$	$0.82^{+0.05}_{-0.06}$
1.1 – 1.3	-0.95	$11.03^{+0.11}_{-0.08}$	$0.20^{+0.05}_{-0.06}$

from $z = 1.2$ down to 0.6 , consistently with the so-called *down-sizing* scenario (Cowie et al. 1996; Fontanot et al. 2009). These new measurements confirm previous evidence, but with a higher statistical reliability. In particular, as we shall discuss in Sect. 4, these estimates have a precision, in terms of Poisson error, that was never reached before at such redshifts by a spectroscopic survey. This improvement is paralleled also by other sources of error, in particular cosmic variance, which we shall discuss in detail in Sects. 3.3 and 3.4.

3.3. Cosmic variance in the VIPERS survey

When dealing with statistical studies using number counts, a severe complication is introduced by the field-to-field fluctuations in the source density, due to the clustered nature of the galaxy distribution and the existence of fluctuations on scales comparable to the survey volume. This sampling or ‘cosmic’ variance represents a further term of uncertainty to be added to the Poisson shot noise. It can be expressed by removing $\sigma_{\text{Pois}}^2 \equiv 1/\langle N \rangle$ from the total relative error:

$$\sigma_{\text{cv}}^2 = \frac{\langle N^2 \rangle - \langle N \rangle^2}{\langle N \rangle^2} - \frac{1}{\langle N \rangle}, \quad (2)$$

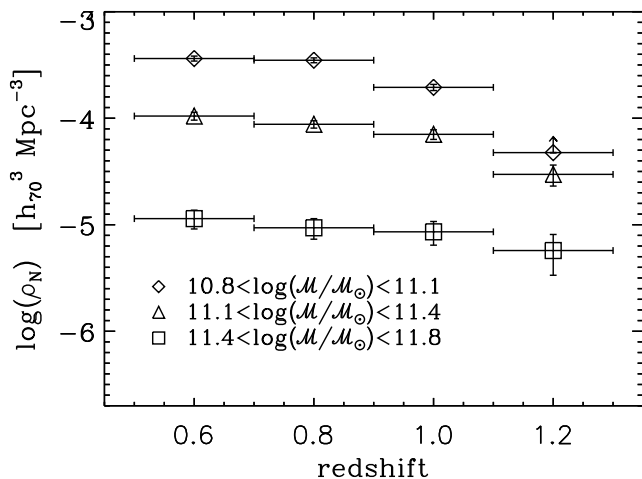


Fig. 5. Evolution of the galaxy number density in different bins of stellar mass. The error bars of the density estimates includes Poisson noise and cosmic variance (see Sect. 3.3). At $z \approx 1.2$, for the lowest-mass sample, only a lower limit can be estimated, indicated by the arrow.

where $\langle N \rangle$ and $\langle N^2 \rangle$ are the mean and the variance of galaxy number counts (Somerville et al. 2004).

Extragalactic pencil-beam surveys, even the deepest ones, are particularly limited by cosmic variance, given the small volume covered per redshift interval. At $z \sim 0.8$, galaxy density fluctuations are found to be still relevant up to a scale of $\sim 140 \text{ Mpc } h_{70}^{-1}$ (Scrimgeour et al. 2012), which roughly corresponds to 5 deg.

This is the result of intrinsic clustering in the matter, as predicted by the power spectrum shape and amplitude at that epoch, amplified by the bias factor of the class of galaxies analysed, which at high redshift can be very large for some classes. For these reasons, even the largest deep surveys of the past generation do not allow us to overcome this issue. For example, the COSMOS field, despite its 2 deg^2 area, turned out to be significantly over-dense between $z = 0.8$ and $z = 1$ (Kovač et al. 2010).

The gain obtained by enlarging the area of a single field beyond a certain coverage becomes less prominent, due to the existing large-scale correlations (see Newman & Davis 2002, Fig. 1): σ_{cv} decreases mildly as a function of volume, with an approximate dependence $\sigma_{\text{cv}} \propto V^{-0.3}$ (Somerville et al. 2004, Fig. 2), compared to $\sigma_{\text{Pois}} \propto V^{-0.5}$. Trenti & Stiavelli (2008) found similar results by characterizing Lyman break galaxies surveys: at high values of $\langle N \rangle$, the Poisson noise rapidly drops and cosmic variance remains the dominant source of uncertainty. A more effective way to abate cosmic variance is to observe separated regions of sky. Since counts in these regions, if they are sufficiently distant, are uncorrelated, their variances sum up in quadrature (i.e., σ_{cv} decreases as the square root of the number of fields, Moster et al. 2011). Multiple independent fields can then result in an uncertainty smaller than a single one, even if the latter has a larger effective area (Trenti & Stiavelli 2008). The current VIPERS PDR-1 sample is not only characterized by a significantly large area (thus volume), compared to previous similar surveys at these redshifts, but this is also split into two independent and well-separated fields of $\sim 7.5 \text{ deg}^2$ each. We therefore expect that the impact of cosmic variance should be limited.

To quantify the impact of cosmic variance directly, we follow two approaches. The first one, based on the observations themselves, provides an upper limit of the VIPERS σ_{cv} . We select five rectangular subregions of about 2 deg^2 within the survey and estimate the mass function Φ_i in each of them, using the $1/V_{\text{max}}$ method described above. We choose non-contiguous regions (separated by $\sim 1 \text{ deg}$) to minimize the covariance between subsamples located within the same field (W1 or W4). Within mass bins $M_j \pm \Delta M/2$ we derive the total random uncertainty

$$\sigma_{\text{tot,obs}}(M_j) = \frac{1}{n} \sum_{i=1}^n \sqrt{[\Phi_i(M_j) - \Phi_{\text{tot}}(M_j)]^2}, \quad (3)$$

where Φ_{tot} is the global GSMF of VIPERS (at that redshift) and $\Phi_i(M_j)$ is the number density of galaxies measured in the j -th mass bin for each of the $n = 5$ subregions.

The second approach is based on the use of simulated mock surveys. First, we use a set of 57 mock samples (26 and 31 in W1 and W4, respectively), built using specific recipes for the stellar-to-halo mass relation. They are based on the MultiDark dark matter simulation (Prada et al. 2012) and have been constructed to reproduce the detailed geometry and selection function of the VIPERS survey (see de la Torre et al. 2013, for details). In that process, the dark matter haloes identified in the simulation, as well as artificial sub-haloes drawn from the Giocoli et al. (2010) sub-halo mass function, have been associated with galaxies using the stellar-to-halo mass relations of Moster et al. (2013). The latter are calibrated on previous stellar mass function measurements in the redshift range $0 < z < 4$. We call these ‘SHMR mocks’. We apply Eq. 2 to estimate the amount of cosmic variance independently among the 26 W1 and 31 W4 mocks. The global estimate of cosmic variance ($\sigma_{\text{cv,SHMR}}$) on the scales of the VIPERS survey is obtained by combining the results from the two fields (see Moster et al. 2011, Eq. 7). As expected, we find that $\sigma_{\text{cv,SHMR}}$ decreases with redshift, since we are probing larger and larger volumes, and increases with stellar mass due to the higher bias factor (and thus higher clustering) of massive galaxies (Somerville et al. 2004). Both the trends are clearly visible in Fig. 6, where measurements of $\sigma_{\text{cv,SHMR}}$ are presented for different bins of redshift and stellar mass.

Besides these SHMR mocks, we also used another set of 50 VIPERS-like light-cones built from the Millennium simulation (Springel et al. 2005), in which dark-matter haloes are populated with galaxies through the semi-analytical model (SAM) of De Lucia & Blaizot (2007). Galaxy properties were determined by connecting the astrophysical processes with the mass accretion history of the simulated dark matter haloes. Each mock sample covers $7 \times 1 \text{ deg}^2$, with a magnitude cut in the i band equal to that of the observed sample. Although the geometry of these mocks (and therefore their volume) slightly differs from the design of the real survey, they provide an independent test, with completely different prescription for galaxy formation, with respect to the SHMR mocks.

In Fig. 6 (crosses), we can notice that the estimates of the standard deviation obtained from the field-to-field fluctuations among the five sub-samples, $\sigma_{\text{tot,obs}}$ have an erratic behaviour and do not show the smooth trend indicated by of $\sigma_{\text{cv,SHMR}}$. The squares should in fact be regarded as an upper limit, given that the subsamples have a volume smaller than the whole survey and since Eq. 3 includes also the variance due to Poisson noise. Conversely, residual correlation among the sub-fields within each of the VIPERS fields (produced by structures on scales $\gtrsim 1 \text{ deg}$ crossing over two or more subregions) would reduce $\sigma_{\text{tot,obs}}$.

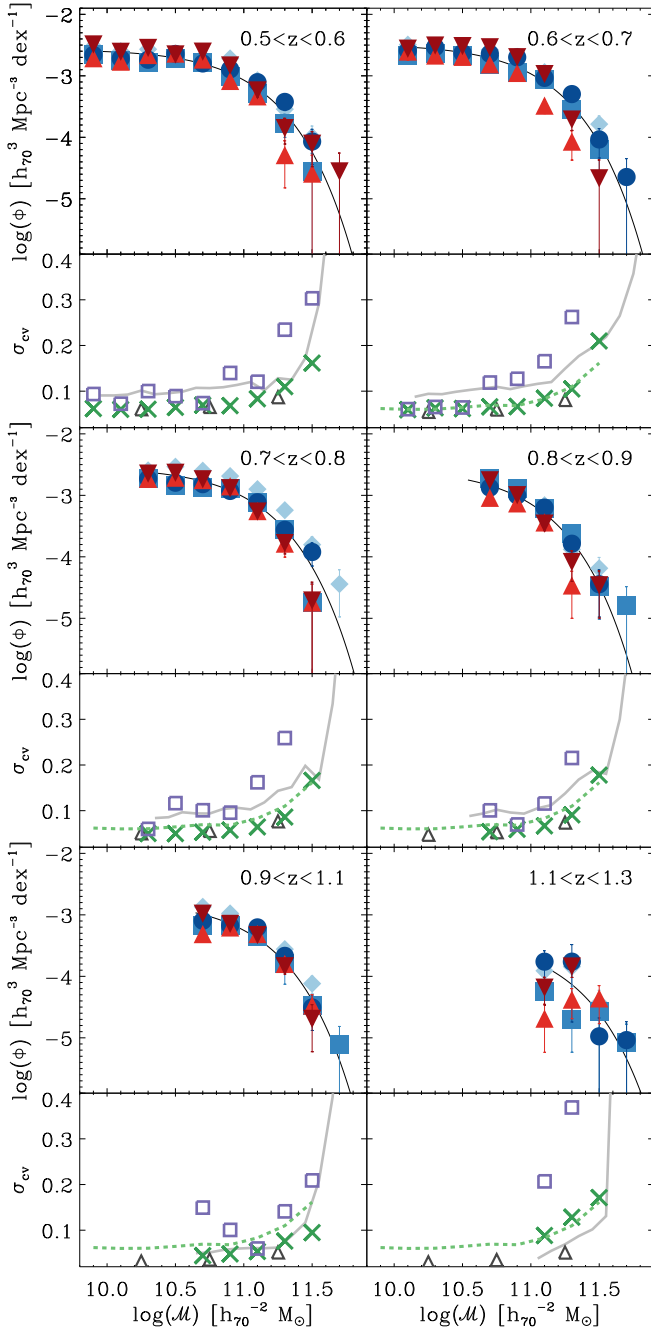


Fig. 6. Estimates of the contribution of sample (cosmic) variance to the statistical uncertainty of the GSMF measurements. For each redshift bin, the upper panels show the GSMF $1/V_{\max}$ measurements obtained from five 2 deg^2 VIPERS subregions, located respectively in the W1 field (three regions, blue diamonds, circles and squares) and in the W4 field (two regions, red triangles and downward triangles). The Schechter fit to the global GSMF of Fig. 4 is shown as reference (black solid line). The lower panels report the standard deviations estimated in each redshift bin from these five measurements (purple squares, Eq. 3), together with the estimates of σ_{cv} obtained from 57 SHMR mocks by means of Eq. 2 (green crosses). To highlight how the effect of cosmic variance decreases at higher z , we report $\sigma_{\text{cv,SHMR}}$ of the first redshift bin in the other panels. In addition, the sample variance measured in 50 SAM mocks (grey solid line) and the estimates provided by Moster et al. (2011) method (black triangles) are shown as reference.

More in general, the small number of fields used to perform this test makes the computation of Eq. 3 statistically uncertain.

In that figure, we also show, as a reference, the estimates provided by the public code `getcv` (Moster et al. 2011) for the same area and redshift bins of the SHMR mocks; these results, limited at $\log(M/M_{\odot}) \leq 11.5$, are in good agreement with $\sigma_{\text{cv,SHMR}}$.

3.4. Other sources of uncertainty

In describing our procedure to derive stellar masses by means of the SED fitting technique (Sect. 2.3), we emphasised the number of involved parameters, and their possible influence on the estimates. The assumptions that have the strongest impact on the results are the choices of the stellar population synthesis model, IMF, SFH, metallicity, and dust extinction law. A thorough discussion about each one of the mentioned ingredients is beyond the goals of this paper, and the reader can refer to Conroy (2013) and Marchesini et al. (2009) for a comprehensive review of the systematic effects induced by the choice of the input parameters.

Here we briefly test the impact on the GSMF of choosing different values of Z (whether including sub-solar metallicities or not), the extinction laws (SB and SMC, or SB alone), and the addition of secondary bursts to the smooth SFHs (i.e. complex SFHs instead of exponentially declining τ -models). We will not modify the other two main ingredients in our procedure, i.e. the universal IMF we assumed (Chabrier 2003) and the stellar population synthesis model (BC03).

To perform this test we use stellar mass estimates obtained by assuming five different sets of SED fitting templates, four of them differing in metallicity and extinction law: Z_{\odot} only and SB; two metallicities (Z_{\odot} and $0.2Z_{\odot}$) and SB; solar metallicity and two extinction laws (SB and SMC); two metallicities (Z_{\odot} and $0.2Z_{\odot}$) and two extinction laws (SB and SMC). The fifth SED fitting estimate has been derived with the *MAGPHYS* code (see Sect. 2.3), assuming the following parameters: complex SFHs, extinction model derived from Charlot & Fall (2000), and a larger range of metallicity (including super-solar ones). We limit these tests to the data in the VIPERS W1 field, i.e. about half of the total sample, given the better overall photometric coverage in this area and the large computational time involved.

The mass functions resulting from these five different SED-modelling assumptions are reported in Fig. 7. As expected (see discussion in Sect. 2.3 and Fig. 1), the *MAGPHYS* mass function corresponds to the highest estimated values of galaxy density at large stellar masses (at least up to $z \approx 1.1$). This trend is not unexpected, because the other four estimates, obtained assuming smooth SFHs templates, are insensitive to an underlying old stellar population that is outshone by a recent burst of star formation (Fontana et al. 2004; Pozzetti et al. 2010, but see Moustakas et al. 2013 for an opposite result). As a consequence, using complex SFHs templates one can produce stellar mass estimates that are larger than those obtained with smooth SFHs for a small percentage of objects, an effect which is more evident in the high-mass tail.

The other estimates, produced by *Hyperzmass*, are in quite good agreement with each other. The mass functions are slightly higher (on average by about 0.1 dex) when obtained using SED fitting procedures that can choose between two values of metallicity. In fact, in this case, red galaxies can be fit with $0.2 Z_{\odot}$ and older ages, consequently resulting in larger stellar mass values. The effect of the extinction law is instead marginal.

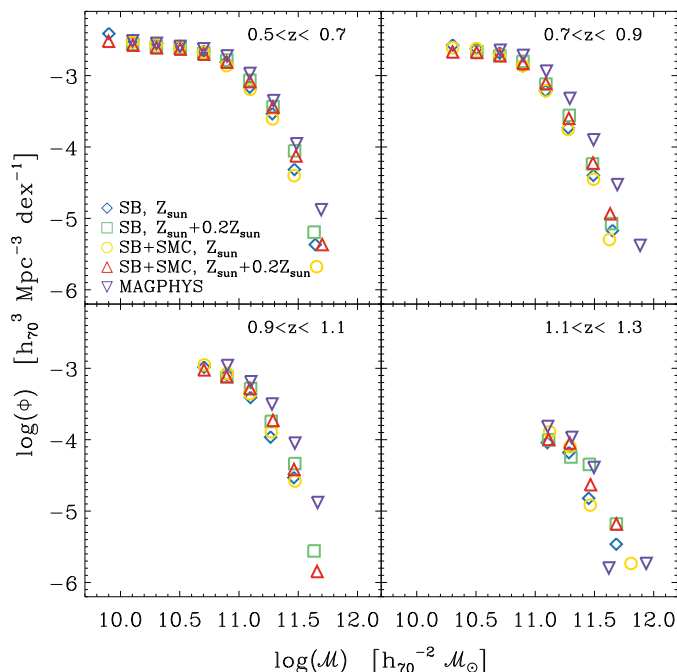


Fig. 7. Dependence of the mass function on the details of the stellar mass estimates, considering five different cases. Specifically, the points correspond to different choices of the stellar population synthesis code, metallicity (Z), extinction law (SB+SMC or SB alone) or the addition of secondary bursts to the smooth star-formation histories. Four cases correspond to SED fitting using *Hyperzmass*, for which the values of the adopted parameters are given at the bottom-left of the first panel. For details about the parameters adopted for *MAGPHYS* (downward triangle), we refer to Sect. 2.3.

4. Comparison to previous work

In this section we compare the VIPERS GSMF with other mass functions derived from different galaxy surveys (Sect. 4.1) and various semi-analytical models (Sect. 4.2). In the present paper we only exploit a sample that is approximately 60% of the final VIPERS catalogue, but this still provides results of a new level of accuracy, especially for the most massive galaxies.

4.1. Comparison with observations

We compare here our estimate of the GSMF with results from other galaxy surveys. We correct GSMFs (if necessary) to be in the same cosmological model with $\Omega_m = 0.3$, $\Omega_b = 0.04$, $h = 0.70$, and Chabrier (2003) IMF. We modify our redshift binning to be similar to other work.

We choose from the literature eight surveys that adopt comparable z -bins, half based on photometric redshifts (Fontana et al. 2006; Pérez-González et al. 2008; Ilbert et al. 2010; Bielby et al. 2012) and half on spectroscopic redshifts (Fontana et al. 2004; Pozzetti et al. 2007, 2010; Moustakas et al. 2013). The spectroscopic redshift sample used by Moustakas et al. (2013) is obtained through a pioneering technique based on a low dispersion prism and slitmasks (see Coil et al. 2011), which results in a precision of $\sigma_z \approx 0.007(1+z)$ (for their high quality sample $Q \geq 3$, see Cool et al. 2013), i.e. comparable to the precision of the best photometric redshifts (Ilbert et al. 2013, who obtain $\sigma_z \approx 0.008(1+z)$ and a very small percentage of outliers).

The redshift ranges of the GSMFs shown in Fig. 8 are $0.4 < z < 0.6$, $0.6 < z < 0.8$, $0.8 < z < 1.0$, with the exception of PRIMUS (Moustakas et al. 2013), which is at $0.5 < z < 0.65$, $0.65 < z < 0.8$, $0.8 < z < 1.0$, and the first bin of VIPERS (i.e., $0.5 < z < 0.6$). In the case of Bielby et al. (2012), who provide the GSMFs in four CFHTLS-Deep quadrants, we do not take into account the results in the D1 field, which is included in W1 field of VIPERS, nor from the D2 field, since in that region we already have two independent estimates (i.e. COSMOS and zCOSMOS Ilbert et al. 2010; Pozzetti et al. 2010). For the VIPERS GSMFs we plot error bars accounting only for σ_{Pois} , i.e. without adding the uncertainty due to cosmic variance, in order to be consistent with most of the literature data, for which only Poisson errors are available.

Our results are in reasonably good agreement with most of the other GSMFs, with the exception of Moustakas et al. (2013), as visible in Fig. 8.

At $0.8 < z < 1.0$, a difference with Ilbert et al. (2010) and Pozzetti et al. (2010) is noteworthy: the likely reason is the presence of a large structure, detected in the COSMOS field (Kovač et al. 2010), demonstrating the importance of the cosmic variance in this kind of comparison.

Some discrepancy remains with the estimates by Moustakas et al. (2013), whose mass functions appear to be systematically higher than all the previous measurements. A possible explanation could be related to the difficulty of estimating statistical weights for the PRIMUS survey: at magnitudes $i \approx 22.5$ the SSR of PRIMUS is approximately 45% and at the limit of the survey it drops below 20% (Cool et al. 2013). Instead, in VIPERS the SSR is $\sim 75\%$ up to our magnitude limit $i = 22.5$ and to $z \approx 1$, making the statistical weight corrections small and very reliable. It is unlikely that the disagreement could be ascribed to cosmic variance, since PRIMUS surveyed a large area, with a number of independent fields (five fields with a total of 5.5 deg^2), which should significantly reduce this problem.

Another source of difference between the observed GSMF in Fig. 8 is the choice of SEDs. Most work has used templates based on the BC03 library (Fontana et al. 2004, 2006; Pozzetti et al. 2007, 2010; Ilbert et al. 2010; Bielby et al. 2012), while Moustakas et al. (2013) derived their reference SEDs according to the stellar synthesis population model by Conroy & Gunn (2010). Pérez-González et al. (2008) also used a different library, selecting their templates from the PEGASE stellar population synthesis model (Fioc & Rocca-Volmerange 1997) and used a training set of ~ 2000 galaxies with spectroscopic z and a wide photometric baseline.

In Fig. 8, the high statistical accuracy of VIPERS can be appreciated with respect to previous spectroscopic surveys. In particular, VIPERS data provide tight constraints on the high-mass end of the GSMF. In fact, previous spectroscopic surveys like K20 and VVDS-Deep (Fontana et al. 2004; Pozzetti et al. 2007, respectively) were unable to probe this portion of the GSMF ($\log(M/M_\odot) \gtrsim 11.5$) because of their relatively small area (52 and 1750 arcmin^2 respectively). Instead, GSMFs derived from photometric redshift surveys are characterised by a Poisson noise that is in general comparable to the level in VIPERS (Pérez-González et al. 2008; Ilbert et al. 2010), but they can be affected by the failures on photometric redshift estimates: even a small fraction of catastrophic redshift measurements can be relevant at large masses (Marchesini et al. 2009, 2010). Moreover, the sky area generally covered by high- z photometric surveys is not large enough for cosmic variance to be negligible.

We will postpone a detailed analysis of the evolution of the local GSMF to a future work: differences in the details of the

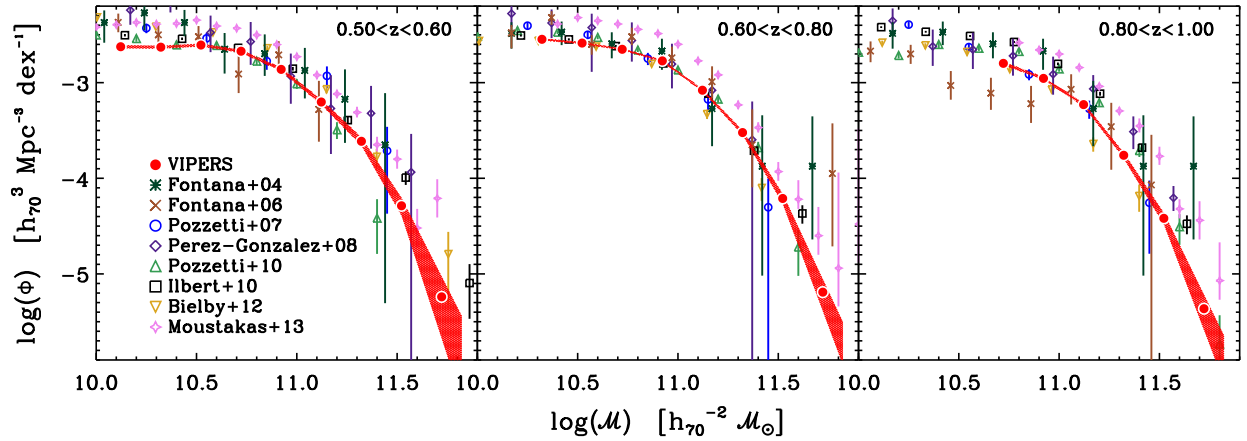


Fig. 8. The VIPERS galaxy stellar mass functions from $z = 0.5$ to 1 (filled red circles, with a red shaded area accounting for the Poisson uncertainty). The $1/V_{\max}$ determinations of previous surveys are also shown by different symbols, along with their respective Poisson error bars. In the left-hand panel, whereas the VIPERS range is $0.5 < z < 0.6$, the other GSMFs are computed between $z = 0.4$ and 0.6 , with the exception of Moustakas et al. (2013) for which is $0.5 < z < 0.65$, $0.65 < z < 0.8$, $0.8 < z < 1.0$; notice the very small error bars of the VIPERS data, despite the narrower redshift range. In the other two panels the bins of VIPERS are the same of the other surveys; also at these higher redshifts the error bars of the VIPERS GSMF are outstanding compared to them.

available estimates from 2dFGRS, SDSS and GAMA (see Cole et al. 2001; Bell et al. 2003; Panter et al. 2004; Baldry et al. 2008; Li & White 2009; Baldry et al. 2012, providing quite different results especially at the massive end) are preventing a robust comparison with our data. Only computing stellar masses and mass functions in a self-consistent way can provide constraints on the evolution of the GSMF down to $z = 0$ (Moustakas et al. 2013).

4.2. Testing models

Besides the comparison with other surveys, it is important to check the agreement of our results with simulations. In this paper we limit ourselves to a preliminary analysis. Nevertheless, this first test provides intriguing results. A future work will be dedicated to more detailed investigations.

The semi-analytical models (SAMs) we consider herein rely on the halo-merger trees of the Millennium Simulation (MS Springel et al. 2005) and the Millennium-II Simulation (MSII Boylan-Kolchin et al. 2009); namely, the MS (comoving box size $L = 714 \text{ Mpc } h_{70}^{-1}$, particle mass $= 1.23 \times 10^9 \text{ } M_{\odot} h_{70}^{-1}$) is used by three of them (Bower et al. 2006; De Lucia & Blaizot 2007; Mutch et al. 2013) while the last one (Guo et al. 2011) is based on the MSII ($L = 143 \text{ Mpc } h_{70}^{-1}$, particle mass $= 9.83 \times 10^6 \text{ } M_{\odot} h_{70}^{-1}$). The tight constraints posed by VIPERS can be very useful when studying whether these models adequately reproduce the real universe.

In Fig. 9, we show the mass functions derived from the models of Bower et al. (2006); De Lucia & Blaizot (2007); Guo et al. (2011), together with the VIPERS results. All the model GSMFs are computed from snapshots at the same redshifts. The narrow redshift binning we can do in VIPERS ($\Delta z = 0.1$) allows us to compare simulated galaxies to observed ones at cosmic times very close to each other. For all of the three SAMs, we observe that the low-mass end of the GSMF is over-estimated. Low-mass galaxies seem to be in place too early. Such a discrepancy, already observed in other work (Somerville et al. 2008; Cirasuolo et al. 2010), is mainly due to an over-predicted fraction of satellite galaxies at those mass scales. This can be caused by an under-efficient supernova feedback and/or some issue in how the star formation efficiency is parametrised at high red-

shifts (Fontanot et al. 2009; Guo et al. 2011). Rescaling the simulations to an up-to-date value of σ_8 (in MS it is equal to 0.9), with the consequence of reducing the small-scale clustering of dark matter haloes, alleviates the tension only in part (Guo et al. 2013).

At higher masses, the VIPERS data provide very tight constraints. At a first glance, De Lucia & Blaizot (2007) and Bower et al. (2006) seem to be in agreement with the observed GSMFs, while the Guo et al. (2011) mass function lies systematically below by ≈ 0.4 dex. However, it should be emphasised that those SAMs do not mimic the observational uncertainties on stellar mass. Adding this kind of error would increase the density of massive objects in the exponential tail of the mass function, and therefore the De Lucia & Blaizot (2007) and Bower et al. (2006) results should be considered at variance with observations also at $\log(M/M_{\odot}) \geq 11$. For this reason we do not show the De Lucia & Blaizot (2007) and Bower et al. (2006) GSMFs convolved with the observational uncertainty on the stellar mass.

The effect of introducing observational uncertainties in the models is shown in Fig. 9 only for the Guo et al. (2011) models, which foresee a lower density of objects in the massive end. We recomputed the Guo et al. GSMFs after convolving stellar masses with a Gaussian of dispersion 0.15 dex. The predictions of Guo et al. (2011) become then in fair agreement with VIPERS. With respect to De Lucia & Blaizot (2007), the main distinguishing features of Guo et al. (2011) are the high efficiency of supernova feedback and a lower rate of gas recycling at low mass. The transition from central to satellite status in the Guo et al. prescription also differs, resulting in a larger number of satellite galaxies than in De Lucia & Blaizot model.

In several recent studies, the parameters of the models we discussed are tuned at $z = 0$ by means of Bayesian approaches, fitting their stellar or luminosity function with data (Henriques et al. 2009; Bower et al. 2010; Lu et al. 2012). Observation at $z > 0$ are then used to verify the model predictions (e.g. Lu et al. 2012). A different kind of calibration has been proposed by Mutch et al. (2013), who modify the input parameters in the SAM of Croton et al. (2006) to match observations at $z = 0$ and $z \approx 0.8$ simultaneously. The VIPERS data will be crucial for such a test. Moreover, thanks to the narrow redshift bins of

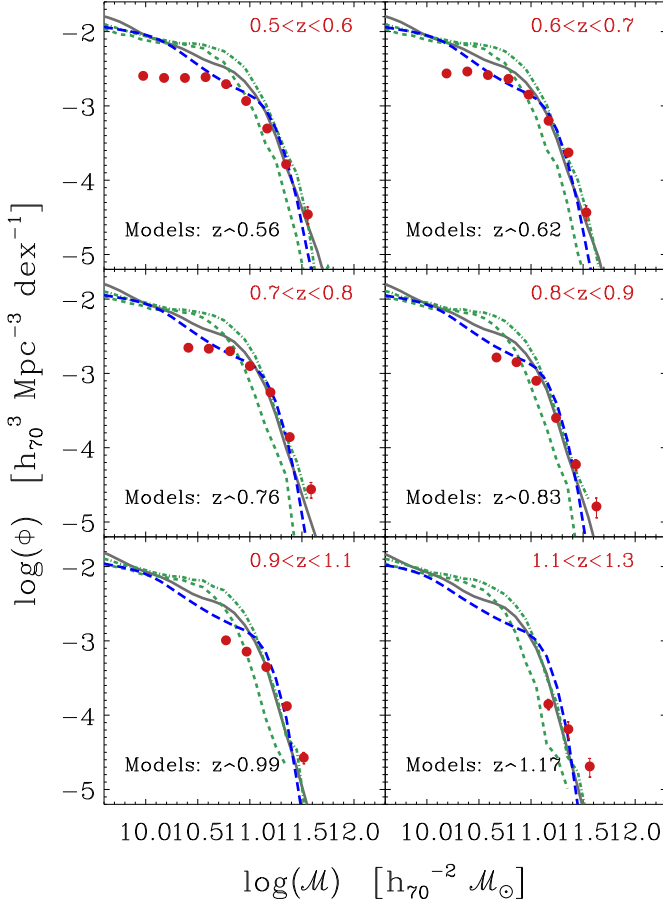


Fig. 9. Comparison of the VIPERS mass function (red points, as in Fig. 4) with the semi-analytical models of De Lucia & Blaizot (2007); Bower et al. (2006); Guo et al. (2011) (grey solid, blue dashed, green short-dashed lines), whose GSMFs have been derived directly from the tables available in the Millennium database (Lemson & Virgo Consortium 2006). The Guo et al. (2011) stellar masses have also been convolved with a Gaussian of dispersion 0.15 dex, to reproduce observational uncertainty on stellar mass determinations; the resulting GSMFs are represented with green dot-dashed lines.

VIPERS, one could precisely characterise the modelled GSMF between $z = 0.5$ and 1, by constraining the SAM parameters in small step of Δz . That method could shed light on the time scale of the physical mechanisms that determine the evolution at higher masses (for instance, the AGN-feedback efficiency).

The results obtained by Mutch et al. (2013) are compared to the VIPERS mass functions in Fig. 10. The plot shows a reasonable agreement beyond $M \simeq 10^{11} M_{\odot}$, not only at the redshift of calibration ($z \simeq 0.83$) but also in the other bins. The authors do not convolve their mass functions with a Gaussian uncertainty on stellar masses, because at least part of the uncertainties this procedure account for should already be included in the observational constraints they use. The Mutch et al. (2013) model is calibrated at $z = 0.83$ by using the results of Pozzetti et al. (2007), Drory et al. (2009), and Ilbert et al. (2010). Among these three GSMFs, only Pozzetti et al. (2007) is based on spectroscopic data (VVDS-Deep), which are unfortunately quite limited at higher masses. The other two estimates (Drory et al. 2009; Ilbert et al. 2010) are derived from the COSMOS survey, which contains a significant over-density at $z \simeq 0.8$. The strategy adopted by Mutch et al. to combine such information may lead to

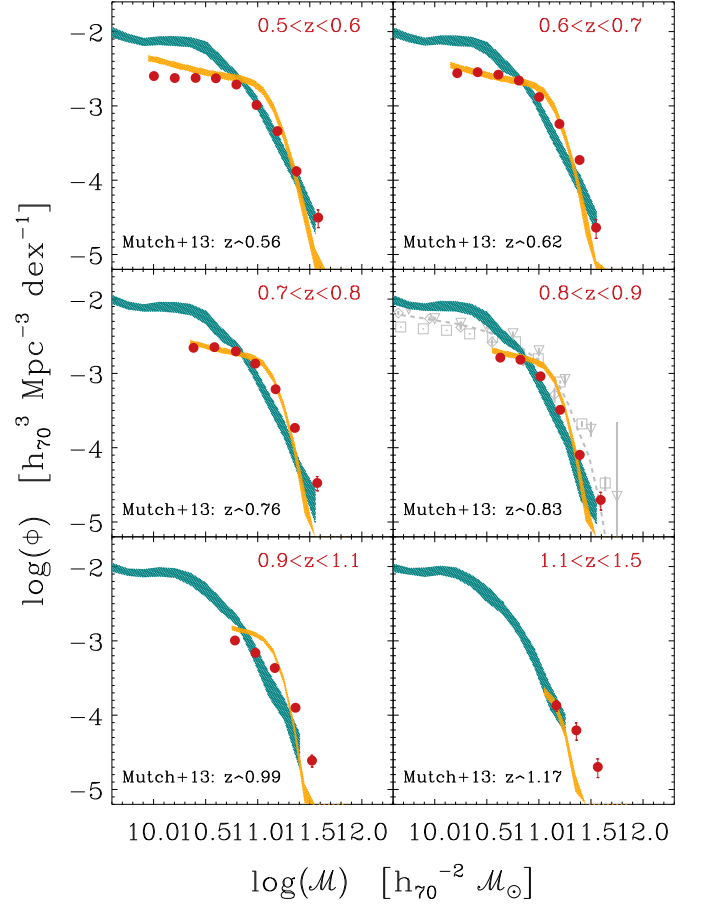


Fig. 10. Comparison of the VIPERS mass function (red points) with the semi-analytical model of Mutch et al. (2013) (green shaded area at 95% confidence limits). In several redshift bins Mutch et al. GSMF does not reach masses as high as VIPERS because the volume of the simulation (with a comoving box size $L = 89.3 \text{ Mpc } h_{70}^{-1}$) is smaller. In the right-hand middle panel ($0.8 < z < 0.9$) it is also shown, with a grey dashed line, the mass function that Mutch et al. obtain by combining observational data from three different surveys (Pozzetti et al. 2007; Drory et al. 2009; Ilbert et al. 2010, grey triangles, diamonds, and squares represent respectively). In addition, the yellow shaded regions represent the dispersion of the mass functions derived from the 57 SHMR mocks (see Sect. 3.3), in the same redshift bins of the VIPERS ones.

overconfidence in the adopted constraints especially in the highest mass range, where observations are most difficult. The observational constraints the authors place on the high-mass end of the model (shown in Fig. 10) could be biased to some extent. To reconcile SAM and observations at $\log(M/M_{\odot}) > 10.8$, Mutch et al. have assumed a star-formation efficiency much higher than the one imposed by Croton et al. (2006), resulting in some tensions concerning the physical prescriptions of the model. Intriguingly, we note that the authors would significantly relieve these tensions if they were to add VIPERS data to their analysis.

From a different perspective, the SHMR mocks we introduced in Sect. 3.3 are also calibrated at multiple z . We decide to test their reliability by deriving their GSMFs (Fig. 10). The agreement is remarkable: VIPERS data confirm the validity of the stellar-to-halo mass relation of Moster et al. (2013) that was used to construct these mocks. This relation connects galaxies with their hosting dark matter halo by means of a redshift-dependent parametrisation that has been calibrated through the

GSMFs of Pérez-González et al. (2008) and Santini et al. (2012) up to $z = 4$. Because of the lack of tight constraints used by Moster et al. for the most massive galaxies (the data from Pérez-González et al. 2008 have lower statistics than ours), the SHMR mass functions diverge at high mass from our estimates.

5. Evolution of the mass function of the red and blue galaxy populations

In order to distinguish the contribution of quiescent and actively star forming galaxies to the global evolution, we now split the sample according to the galaxy rest-frame ($U - V$) colour (see Fritz et al. (2013) for extensive discussion).

5.1. Classification of galaxy types

The absolute magnitudes for galaxies in the VIPERS catalogue were computed from the same SED fitting procedure described in Sect. 2.3, applying a k - and colour-correction, derived from the best fit SED, to the apparent magnitudes in the bands that more closely match the rest-frame emission in the U and V filters (see Fritz et al. 2013, for details). In this way, ($U - V$) rest-frame colours can be reliably computed within the redshift range of the survey, evidencing the classical bimodality (Fritz et al. 2013) and allowing us to separate red-sequence from blue-cloud galaxies (Strateva et al. 2001; Hogg et al. 2002; Bell et al. 2004).

The valley between the two populations is found to be slightly evolving toward bluer colours at earlier epochs. This photometric classification, despite its simplicity, can be considered as a good proxy for the selection of quiescent and star-forming galaxies, as discussed by Mignoli et al. (2009) using zCOSMOS data: 86% (93%) of the galaxies selected as being photometrically red (blue) are also quiescent (star-forming) as defined from their spectra.

To verify and validate our selection method, we also derive galaxy photometric types by fitting our photometry with the empirical set of 62 templates used in Ilbert et al. (2006), which was optimised as to refine the match between photometric and spectroscopic redshifts in the VVDS. The same set was also used to classify galaxies in several other papers (e.g. Zucca et al. 2006, 2009; Pozzetti et al. 2010; Moresco et al. 2010). The classification of VIPERS galaxies resulting from this second method, matches reasonably well with the ($U - V$) colour selection. More than 70% of the red galaxies are defined as early-type objects by the SED analysis, while more than 95% of blue galaxies are classified as late-types. For red galaxies this worsen beyond $z = 1.1$, where only 55% of the red galaxies are classified as early-type in terms of their SED. In the same redshift range, instead, 98% of blue galaxies are classified as late-type objects.

5.2. Blue and red galaxy stellar mass functions

Using this classification, we are now in the position to quantify the contribution of red and blue galaxies to the GSMF and in particular to its high-mass end. The results are shown in Fig. 11. The mass functions for each class are estimated in bins of 0.2 in $\log(M_\odot)$, using the same $1/V_{\max}$ method described in Sect. 3.2. Fits with the usual Schechter function are provided, as described in the caption, to highlight evolution (or absence thereof) as a function of redshift.

The predominance of red (passive) objects among the massive galaxies is clearly visible in all redshift bins, with blue (active) galaxies mainly contributing at lower masses ($M < M_\star$).

Since the mass completeness limit M_{\lim} for the blue population extends to sufficiently small masses, we can perform the Schechter fit letting M_\star , Φ_\star , and α free. The slope of the low-mass end remains almost constant in redshift for the blue population, with $1.2 < \alpha < 1.3$, up to $z \simeq 0.9$, as seen in previous works (cf. Pozzetti et al. 2010). At redshift larger than this it can no longer be constrained. Because of the high values of the mass completeness limit M_{\lim} for the red population (see Sect. 3.1), it is not possible to study the red sample in the same range, e.g. determining the evolution of α (Ilbert et al. 2010) or a possible upturn of the GSMF (cf. Drory et al. 2009).

From these measurements we can determine the value of M_{cross} , where the blue and red GSMFs intersect, i.e. the dividing line between the ranges in which blue and red galaxies respectively dominate the mass function (Kauffmann et al. 2003b). The physical meaning of M_{cross} has been questioned (Bell et al. 2007), but it is in general considered as a proxy to the transition mass of physical processes such the quenching of star formation, (responsible for the migration from the blue cloud to the red sequence), or the AGN activity (e.g. Kauffmann et al. 2003a). Moreover, its clear dependence on environment (Bolzonella et al. 2010) points to an interpretation of the galaxy transformation linked not only to secular processes.

We quantify the value of the transition mass in each redshift bin using the $1/V_{\max}$ measurements. The transition mass increases from $\log(M_{\text{cross}}/M_\odot) = 10.4$ at $z \simeq 0.55$ to $\log(M_{\text{cross}}/M_\odot) = 10.6$ at $z \simeq 0.75$, as shown in Fig. 12. This trend is very well fitted by a power law $\propto (1+z)^3$. Beyond $z = 0.8$ our M_{cross} estimates (open circles) should be formally considered as upper limits, since they fall below the mass completeness limit of red galaxies, but at least up to $z = 1.0$ they can be considered as a good approximation of the real values, given their proximity to the limit.

In Fig. 12 we also plot results from previous studies. In this respect, it is important to underline that the value of the completeness mass M_{cross} provided by the various authors can differ significantly from each other, depending on the adopted classification. For instance, the results of the morphological classification used by Bundy et al. on the DEEP2 survey fall outside of the mass ranges considered in the plot. This could be related to part of the “red and dead” galaxies at such redshifts becoming ellipticals (in morphological sense) at a later stage (Bundy et al. 2010). In fact, when we split the DEEP2 sample on the basis of the ($U - B$) bimodality (upper half-circles), the results are then in agreement with our findings. Our estimates of M_{cross} are fairly consistent with those of Vergani et al. (2008), Pozzetti et al. (2010), Moustakas et al. (2013). The estimates by Vergani et al. (2008) (asterisks in Fig. 12), rely on the identification of the D4000 break in the VVDS spectra and have a steeper redshift evolution, $M_{\text{cross}} \propto (1+z)^4$. Pozzetti et al. (2010) derived M_{cross} from the GSMFs of the zCOSMOS (10k-bright) sample split using different criteria: a cut in specific SFR (i.e. $s\text{SFR} \equiv \text{SFR}/M \gtrsim 10^{-1} \text{ Gyr}^{-1}$ – open squares in the plot), morphology (spheroidal vs disc/irregular galaxies – diamonds), and best-fit SEDs (same photometric types discussed in Sect. 5.1 – triangles). Moustakas et al. (2013) define star-forming galaxies as lying in the so-called main sequence of the SFR (estimated from the SED fitting) vs M diagram (Noeske et al. 2007). They find a flatter evolution, with $M_{\text{cross}} \propto (1+z)^{1.5}$ (dashed line).

5.3. Evolution of the blue and red populations

To study the processes of star formation quenching that cause the transition of galaxies from the so-called blue cloud to the

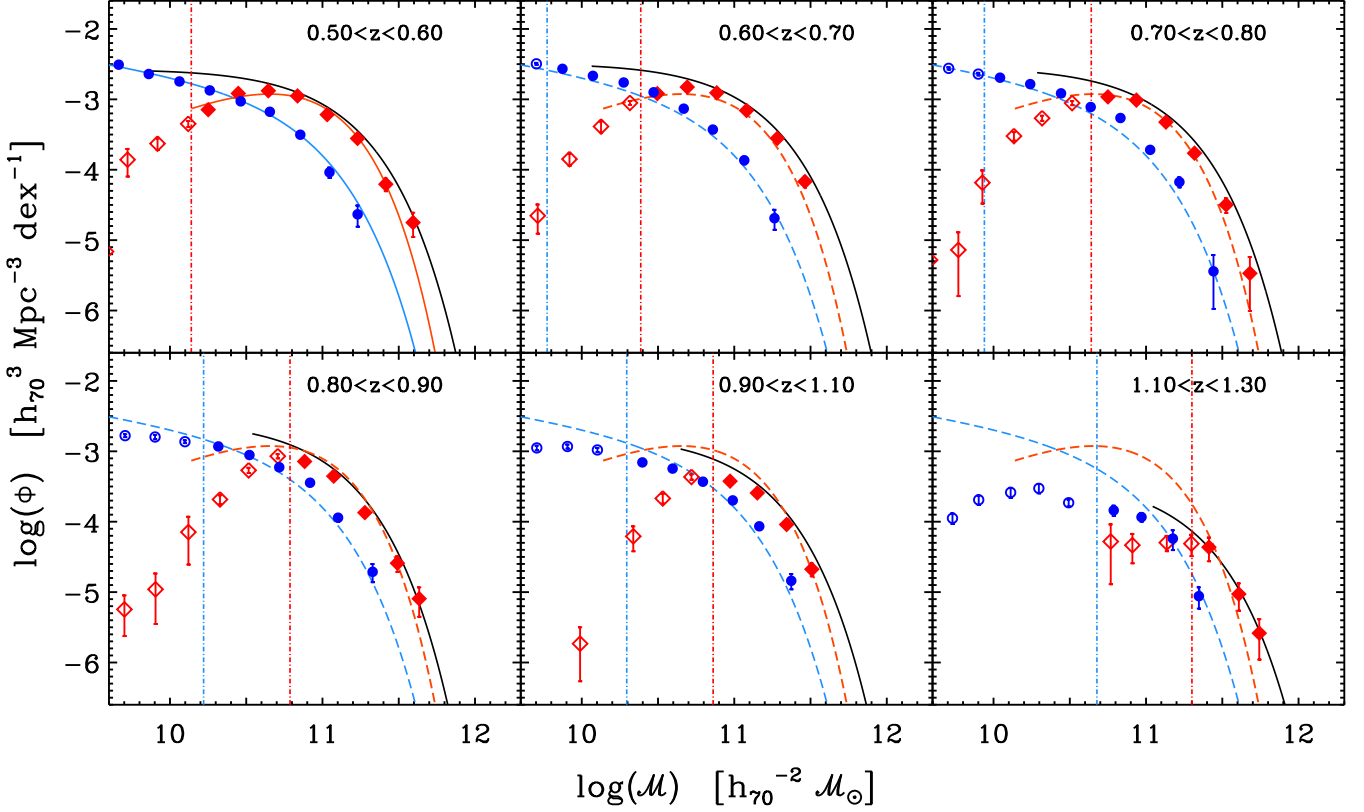


Fig. 11. The galaxy stellar mass functions of the blue and red populations in VIPERS, derived using the $1/V_{\max}$. Symbols (circles and diamonds respectively) are filled for data above the corresponding completeness limit M_{lim} (vertical lines) and empty below. Error bars account for Poisson noise only. The Schechter fit of the two populations in the bin $0.5 < z < 0.6$ (solid blue and red lines) is reported for reference as a dashed line in the other panels. The solid black line in each panel give the Schechter best-fit to the whole VIPERS sample in that redshift bin.

red sequence (Faber et al. 2007), we measured the evolution of the galaxy number density of blue and red populations, namely $\rho_N^{\text{blue}}(z)$ and $\rho_N^{\text{red}}(z)$. These estimates are derived using the $1/V_{\max}$ method, taking into account both Poisson noise and cosmic variance. We also verified, however, that the results would be essentially the same if we had measured number densities by integrating the Schechter best-fitting functions. We explore four narrow bins of stellar mass to highlight the dependence of the quenching processes on this parameter. To improve statistics at large stellar masses, here we choose wider redshift bins: $0.5\text{--}0.7$, $0.7\text{--}0.9$, $0.9\text{--}1.1$, $1.1\text{--}1.3$ (the same used by Fritz et al. 2013, for the analysis of the VIPERS luminosity function).

At intermediate masses ($10.8 < \log(M/M_\odot) < 11.1$) the number density of red galaxies ρ_N^{red} increases by a factor of ~ 2.5 from $z = 1$ to $z = 0.6$, whereas at higher masses the variation is much smaller: red galaxies with mass $11.1 < \log(M/M_\odot) < 11.4$ evolve from a number density $\rho_N^{\text{red}} = (5.3 \pm 0.6) \times 10^{-5} \text{ Mpc}^{-3} h_{70}^3$ to $(9.5 \pm 1.1) \times 10^{-5} \text{ Mpc}^{-3} h_{70}^3$ in the same redshift interval (about 80% increase). This result is in line with the mass-assembly downsizing scenario highlighted in previous works (Cimatti et al. 2006; Pozzetti et al. 2010; Ilbert et al. 2010): elliptical galaxies with $M > 10^{11} M_\odot$ built their stellar mass well before the less massive ones. With the VIPERS data we are able for the first time to provide significant evidence of this trend for such massive galaxies $\log(M/M_\odot) \geq 11.4$ at these redshifts. Thanks to the combination of large volume and sampling of VIPERS we can look for evolutionary trends in this mass range, without being affected by the cosmic variance. We find that the number density of the most massive red galaxies

in our redshift range increases by 45%, confirming that they did not experience a strong evolution between $z \approx 1.2$ and $z \approx 0.6$. Quenching mechanisms seem to be more efficient at low and intermediate masses, as recently suggested also by Moustakas et al. (2013). With respect to PRIMUS, the VIPERS survey extends this finding to higher masses ($\log(M/M_\odot) > 11.4$) and redshifts (up to ≈ 1.2). The evidence of mass dependence of quenching is in agreement with Peng et al. (2010), although other mechanisms could play a non-negligible role (e.g. galaxy mergers, Xu et al. 2012).

The co-moving number density of blue galaxies, instead, is found to be relatively stable between $z \approx 1$ to $z \approx 0.6$ for objects with mass $10.5 \leq \log(M/M_\odot) < 10.8$, with a 10% variation. For larger-mass blue galaxies, for which the sample is complete at all redshifts, the density ρ_N^{blue} of objects with mass $10.8 \leq \log(M/M_\odot) < 11.1$ shows indications for a mild increase between $z \approx 1.2$ and $z = 0.8$.

The most massive blue galaxies ($\log(M/M_\odot) \geq 11.4$) disappear downward of $z \approx 0.6$ (see the right panel in Fig. 13), giving us a hint about the time at which the stellar mass cut-off of active galaxies developed. When the whole VIPERS sample will be available, we will carry on the analysis of the massive end buildup with more robust statistics. Moreover, a step forward for a better comprehension of this picture will be the use of spectral features to determine reliable estimates of the SFR, and therefore to better separate passive and active galaxies.

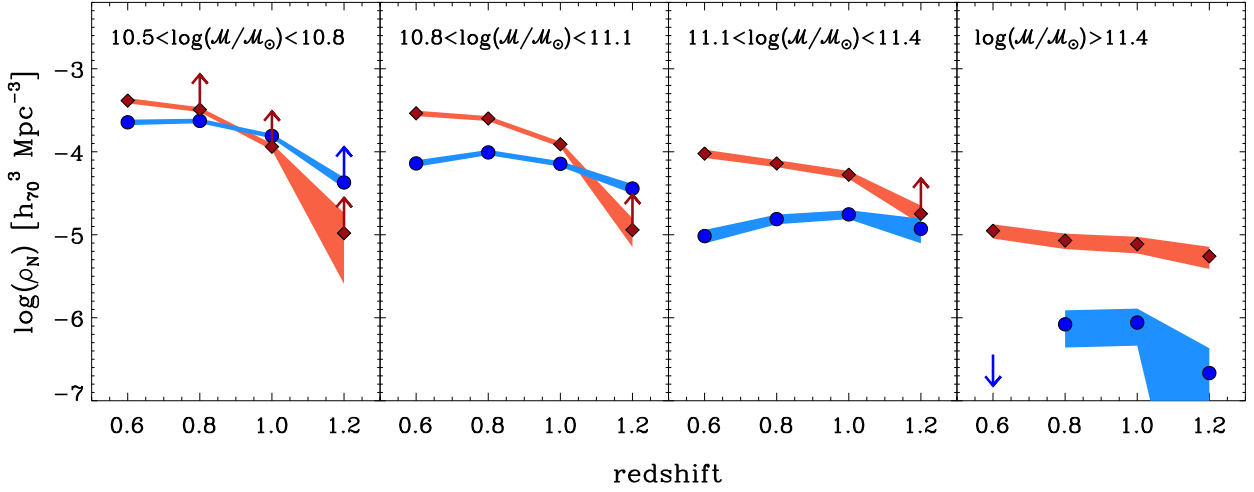


Fig. 13. Evolution of the abundance (number density) of the blue and red galaxy populations with different stellar masses in VIPERS (filled circles and diamonds respectively). The error corridors reflect the overall uncertainties, which include both Poisson noise and cosmic variance added in quadrature.

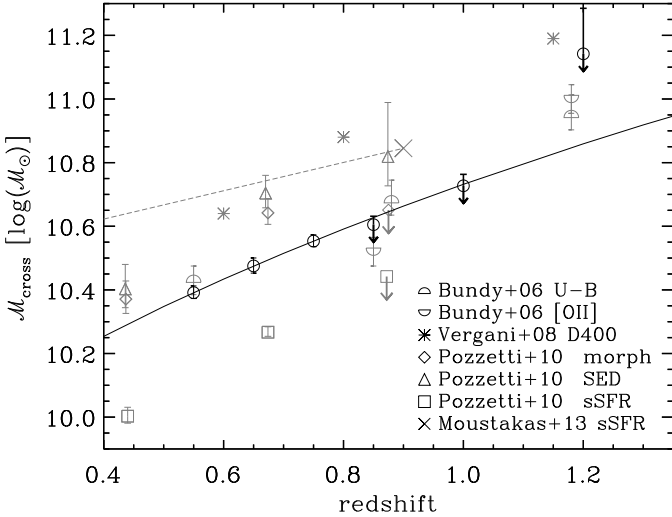


Fig. 12. The values of the transition mass M_{cross} as computed from Fig. 11, plotted as a function of redshift. The VIPERS measurements are given as black open circles, with a downward arrow depending on whether the transition mass is above or below the completeness mass of at least one of the two classes. The solid line is a fit with a $(1+z)^3$ power-law to the VIPERS points between $z = 0.5$ and $z = 0.8$. These are compared to literature estimates in grey. Points from Pozzetti et al. (2010) are obtained using three different classifications: a separation according to specific SFR (diamonds), a best-fit SED classification (triangles), and a morphological classification (squares). The points of Bundy et al. (2006) are based on the $(U-B)$ bimodality and [OII] emission respectively (see text). The points by Vergani et al. (2008) are based on a spectral classification (D4000 break). The value from PRIMUS (Moustakas et al. 2013) at $z = 0.9$ is reported as a cross, while the dashed line traces an evolution $\propto (1+z)^{1.5}$, as suggested in that paper; these authors classified active and quiescent galaxies with respect to their position in the SFR vs M diagram.

6. Conclusions

We have measured the GSMF between $z = 0.5$ and $z = 1.3$ using the first data release of VIPERS. The forthcoming VIPERS

Public Data Release 1 (PDR-1) will contain the catalogue of the 53 608 spectroscopic galaxy redshifts used in the present analysis. The galaxy stellar masses have been estimated through an SED fitting technique, relying on a large photometric baseline, and in particular on a nearly full coverage of our fields with near-infrared data; we performed several tests to verify that the systematics intrinsic to the method of SED fitting (e.g. the parametrisation of the SFH) are not introducing any bias in our analysis. The large volume probed by VIPERS results in extremely high statistics, dramatically reducing the uncertainties due to Poisson noise (σ_{Pois}) and sample variance (σ_{cv}). We estimate the latter by using 57 galaxy mock catalogues based on the MultiDark simulation (Prada et al. 2012) and the stellar-to-halo mass relation of Moster et al. (2013). These mocks closely reproduce the characteristics of the VIPERS survey.

We empirically determined a completeness threshold M_{lim} above which the mass function can be considered complete: this limiting mass evolves as a function of z , ranging from $\log(M/M_{\odot}) = 9.8$ to 11 in the redshift interval 0.5–1.1. We focused our analysis on the high-mass end of the GSMF, where VIPERS detects a particularly high number of rare massive galaxies. The main results we obtain are:

- VIPERS data tightly constrain the exponential tail of the Schechter function, which does not show significant evolution at high masses below $z = 1.1$. The same result is provided by the analysis of the co-moving number density ρ_N , calculated in different bins of stellar mass: at $z \approx 1.2$ most of the massive galaxies with $\log(M/M_{\odot}) \geq 11.4$ are already in place, whereas below $\log(M/M_{\odot}) = 11.4$ the galaxy number density increases by a factor of ~ 3.5 from $z \approx 1.2$ to $z \approx 0.6$.
- We compare our observed GSMFs with those derived from semi-analytical models (De Lucia & Blaizot 2007; Bower et al. 2006; Guo et al. 2011). While the discrepancy at low masses between models and observations is well established and has been exhaustively discussed in literature, predictions at the high-mass end of the GSMF have not yet been verified with sufficient precision. We show that the high accuracy of the VIPERS mass functions make them suitable for this kind of tests. From a first analysis, the VIPERS data appear to be

consistent with the Guo et al. (2011) model, once the uncertainties in the stellar mass estimates are taken into account. A more detailed analysis will be the subject of a future work. We suggest that VIPERS GSMFs can be effectively used to constrain models at multiple redshifts simultaneously, as pioneered in the work of Mutch et al. (2013).

- We divide the VIPERS sample by means of a colour criterion based on the $(U - V)$ bimodality (Fritz et al. 2013) and we estimate the blue and red GSMF in the same range, $0.5 < z < 1.3$. We find that the transition mass above which the GSMF is dominated by red galaxies is about $10^{10.4} M_{\odot}$ at $z \approx 0.55$ and evolves proportional to $(1 + z)^3$.
- The number density of the red sample shows an evolution that depends on stellar mass, being steeper at lower masses. At large stellar masses the quenching of active galaxies has not been thoroughly studied, because of the poor sample statistics. We obtain a first impressive result with VIPERS, detecting at $z \approx 1$ a significant number of very massive active galaxies with $\log(M/M_{\odot}) \geq 11.4$, which have all migrated onto the red sequence by $z = 0.6$, i.e. in about 2 Gyr.

The first data release of VIPERS has thus allowed us to study the evolution of the galaxy stellar mass function over an unprecedented volume at redshifts $z = 0.5 - 1.3$. We emphasise the constraining power of this dataset, particularly for the abundance of the most massive galaxies, both quiescent and star-forming. In forthcoming studies we will make full use of the growing sample and of the measurement of spectral features, in order to investigate the cosmic star formation history and confront galaxy formation models at high redshift.

Acknowledgements. We are grateful to Lucia Pozzetti for useful suggestions and for providing us zCOSMOS results. We thank Simon J. Mutch who provided us the GSMF foreseen by the model described in Mutch et al. (2013) in our preferred redshift bins. ID warmly thanks Ivan Delvecchio for useful discussions. We acknowledge the crucial contribution of the ESO staff for the management of service observations. In particular, we are deeply grateful to M. Hilker for his constant help and support of this program. Italian participation to VIPERS has been funded by INAF through PRIN 2008 and 2010 programs. LG and BRG acknowledge support of the European Research Council through the Darklight ERC Advanced Research Grant (# 291521). OLF acknowledges support of the European Research Council through the EARLY ERC Advanced Research Grant (# 268107). Polish participants have been supported by the Polish Ministry of Science (grant N N203 51 29 38), the Polish-Swiss Astro Project (co-financed by a grant from Switzerland, through the Swiss Contribution to the enlarged European Union), the European Associated Laboratory Astrophysics Poland-France HECOLS and a Japan Society for the Promotion of Science (JSPS) Postdoctoral Fellowship for Foreign Researchers (P11802). GDL acknowledges financial support from the European Research Council under the European Community's Seventh Framework Programme (FP7/2007-2013)/ERC grant agreement n. 202781. WJP and RT acknowledge financial support from the European Research Council under the European Community's Seventh Framework Programme (FP7/2007-2013)/ERC grant agreement n. 202686. WJP is also grateful for support from the UK Science and Technology Facilities Council through the grant ST/I001204/1. EB, FM and LM acknowledge the support from grants ASI-INAF I/023/12/0 and PRIN MIUR 2010-2011. YM acknowledges support from CNRS/INSU (Institut National des Sciences de l'Univers) and the Programme National Galaxies et Cosmologie (PNCG). CM is grateful for support from specific project funding of the *Institut Universitaire de France* and the LABEX OCEVU.

References

- Baldry, I. K., Driver, S. P., Loveday, J., et al. 2012, *MNRAS*, 421, 621
 Baldry, I. K., Glazebrook, K., & Driver, S. P. 2008, *MNRAS*, 388, 945
 Barro, G., Faber, S. M., Pérez-González, P. G., et al. 2013, *ApJ*, 765, 104
 Behroozi, P. S., Wechsler, R. H., & Conroy, C. 2013, *ApJ*, 762, L31
 Bel, J. et al. 2013, *A&A* submitted
 Bell, E. F., McIntosh, D. H., Katz, N., & Weinberg, M. D. 2003, *ApJS*, 149, 289
 Bell, E. F., Wolf, C., Meisenheimer, K., et al. 2004, *ApJ*, 608, 752
 Bell, E. F., Zheng, X. Z., Papovich, C., et al. 2007, *ApJ*, 663, 834
 Bertin, E. & Arnouts, S. 1996, *A&AS*, 117, 393
 Bielby, R., Hudelot, P., McCracken, H. J., et al. 2012, *A&A*, 545, A23
 Blanton, M. R., Lupton, R. H., Schlegel, D. J., et al. 2005, *ApJ*, 631, 208
 Bolzonella, M., Kovač, K., Pozzetti, L., et al. 2010, *A&A*, 524, A76
 Bolzonella, M., Miralles, J.-M., & Pelló, R. 2000, *A&A*, 363, 476
 Borch, A., Meisenheimer, K., Bell, E. F., et al. 2006, *A&A*, 453, 869
 Bouchet, P., Lequeux, J., Maurice, E., Prevot, L., & Prevot-Burnichon, M. L. 1985, *A&A*, 149, 330
 Bower, R. G., Benson, A. J., Malbon, R., et al. 2006, *MNRAS*, 370, 645
 Bower, R. G., Vernon, I., Goldstein, M., et al. 2010, *MNRAS*, 407, 2017
 Boylan-Kolchin, M., Springel, V., White, S. D. M., Jenkins, A., & Lemson, G. 2009, *MNRAS*, 398, 1150
 Bruzual, G. & Charlot, S. 2003, *MNRAS*, 344, 1000
 Bundy, K., Ellis, R. S., Conselice, C. J., et al. 2006, *ApJ*, 651, 120
 Bundy, K., Scarlata, C., Carollo, C. M., et al. 2010, *ApJ*, 719, 1969
 Calzetti, D., Armus, L., Bohlin, R. C., et al. 2000, *ApJ*, 533, 682
 Chabrier, G. 2003, *PASP*, 115, 763
 Charlot, S. & Fall, S. M. 2000, *ApJ*, 539, 718
 Cimatti, A., Daddi, E., & Renzini, A. 2006, *A&A*, 453, L29
 Cirasuolo, M., McLure, R. J., Dunlop, J. S., et al. 2010, *MNRAS*, 401, 1166
 Coil, A. L., Blanton, M. R., Burles, S. M., et al. 2011, *ApJ*, 741, 8
 Cole, S., Norberg, P., Baugh, C. M., et al. 2001, *MNRAS*, 326, 255
 Conroy, C. 2013, *ArXiv e-prints*
 Conroy, C. & Gunn, J. E. 2010, *ApJ*, 712, 833
 Conroy, C., Gunn, J. E., & White, M. 2009, *ApJ*, 699, 486
 Conseil, S., Vibert, D., Amouts, S., et al. 2011, in *Astronomical Society of the Pacific Conference Series*, Vol. 442, *Astronomical Data Analysis Software and Systems XX*, ed. I. N. Evans, A. Accomazzi, D. J. Mink, & A. H. Rots, 107
 Cool, R. J., Moustakas, J., Blanton, M. R., et al. 2013, *ArXiv e-prints*
 Coupon, J., Ilbert, O., Kilbinger, M., et al. 2009, *A&A*, 500, 981
 Cowie, L. L., Songaila, A., Hu, E. M., & Cohen, J. G. 1996, *AJ*, 112, 839
 Croton, D. J., Springel, V., White, S. D. M., et al. 2006, *MNRAS*, 365, 11
 Cucciati, O., Iovino, A., Kovac, K., et al. 2010, *ArXiv e-prints*
 da Cunha, E., Charlot, S., & Elbaz, D. 2008, *MNRAS*, 388, 1595
 de la Torre, S., Guzzo, L., Peacock, J. A., et al. 2013, *ArXiv e-prints*
 De Lucia, G. & Blaizot, J. 2007, *MNRAS*, 375, 2
 Dickinson, M., Papovich, C., Ferguson, H. C., & Budavári, T. 2003, *ApJ*, 587, 25
 Drory, N., Bundy, K., Leauthaud, A., et al. 2009, *ApJ*, 707, 1595
 Faber, S. M., Willmer, C. N. A., Wolf, C., et al. 2007, *ApJ*, 665, 265
 Felten, J. E. 1976, *ApJ*, 207, 700
 Fioc, M. & Rocca-Volmerange, B. 1997, *A&A*, 326, 950
 Fontana, A., Donnarumma, I., Vanzella, E., et al. 2003, *ApJ*, 594, L9
 Fontana, A., Pozzetti, L., Donnarumma, I., et al. 2004, *A&A*, 424, 23
 Fontana, A., Salimbeni, S., Grazian, A., et al. 2006, *A&A*, 459, 745
 Fontanot, F., De Lucia, G., Monaco, P., Somerville, R. S., & Santini, P. 2009, *MNRAS*, 397, 1776
 Franx, M., van Dokkum, P. G., Schreiber, N. M. F., et al. 2008, *ApJ*, 688, 770
 Fritz, A. et al. 2013, *A&A* submitted
 Gabor, J. M., Davé, R., Finlator, K., & Oppenheimer, B. D. 2010, *MNRAS*, 407, 749
 Garilli, B., Fumana, M., Franzetti, P., et al. 2010, *PASP*, 122, 827
 Garilli, B., Paioro, L., Scoddeggio, M., et al. 2012, *PASP*, 124, 1232
 Gehrels, N. 1986, *ApJ*, 303, 336
 Giocoli, C., Tormen, G., Sheth, R. K., & van den Bosch, F. C. 2010, *MNRAS*, 404, 502
 Granett, B. R., Guzzo, L., Coupon, J., et al. 2012, *MNRAS*, 421, 251
 Guillaume, M., Llebaria, A., Aymeric, D., Arnouts, S., & Milliard, B. 2006, in *Society of Photo-Optical Instrumentation Engineers (SPIE) Conference Series*, Vol. 6064, *Society of Photo-Optical Instrumentation Engineers (SPIE) Conference Series*, ed. E. R. Dougherty, J. T. Astola, K. O. Egiazarian, N. M. Nasrabadi, & S. A. Rizvi, 332–341
 Guo, Q., White, S., Angulo, R. E., et al. 2013, *MNRAS*, 428, 1351
 Guo, Q., White, S., Boylan-Kolchin, M., et al. 2011, *MNRAS*, 413, 101
 Guzzo, L., Scoddeggio, M., Garilli, B., et al. 2013, *ArXiv e-prints*
 Henriques, B. M. B., Thomas, P. A., Oliver, S., & Roseboom, I. 2009, *MNRAS*, 396, 535
 Hogg, D. W., Blanton, M., Strateva, I., et al. 2002, *AJ*, 124, 646
 Ilbert, O., Arnouts, S., McCracken, H. J., et al. 2006, *A&A*, 457, 841
 Ilbert, O., Capak, P., Salvato, M., et al. 2009, *ApJ*, 690, 1236
 Ilbert, O., McCracken, H. J., Le Fevre, O., et al. 2013, *ArXiv e-prints*
 Ilbert, O., Salvato, M., Le Floc'h, E., et al. 2010, *ApJ*, 709, 644
 Ilbert, O., Tresse, L., Zucca, E., et al. 2005, *A&A*, 439, 863
 Iovino, A., Cucciati, O., Scoddeggio, M., et al. 2010, *A&A*, 509, A40+
 Kajisawa, M., Ichikawa, T., Tanaka, I., et al. 2009, *ApJ*, 702, 1393
 Kauffmann, G., Heckman, T. M., White, S. D. M., et al. 2003a, *MNRAS*, 341, 33
 Kauffmann, G., Heckman, T. M., White, S. D. M., et al. 2003b, *MNRAS*, 341, 54
 Kovač, K., Lilly, S. J., Cucciati, O., et al. 2010, *ApJ*, 708, 505

Kriek, M., Labbé, I., Conroy, C., et al. 2010, *ApJ*, 722, L64

Kroupa, P. 2001, *MNRAS*, 322, 231

Le Fèvre, O., Vettolani, G., Garilli, B., et al. 2005, *A&A*, 439, 845

Lee, S.-K., Idzi, R., Ferguson, H. C., et al. 2009, *ApJS*, 184, 100

Lemson, G. & Virgo Consortium, t. 2006, *ArXiv Astrophysics e-prints*

Li, C. & White, S. D. M. 2009, *MNRAS*, 398, 2177

Lilly, S. J., Le Brun, V., Maier, C., et al. 2009, *ApJS*, 184, 218

Lin, L., Koo, D. C., Weiner, B. J., et al. 2007, *ApJ*, 660, L51

Lu, Y., Mo, H. J., Katz, N., & Weinberg, M. D. 2012, *MNRAS*, 421, 1779

MacArthur, L. A., McDonald, M., Courteau, S., & Jesús González, J. 2010, *ApJ*, 718, 768

Malek, K., Solarz, A., Pollo, A., et al. 2013, *ArXiv e-prints*

Maraston, C. 2005, *MNRAS*, 362, 799

Maraston, C., Daddi, E., Renzini, A., et al. 2006, *ApJ*, 652, 85

Maraston, C., Pforr, J., Henriques, B. M., et al. 2012, *ArXiv e-prints*

Maraston, C., Pforr, J., Renzini, A., et al. 2010, *MNRAS*, 407, 830

Marchesini, D., van Dokkum, P. G., Förster Schreiber, N. M., et al. 2009, *ApJ*, 701, 1765

Marchesini, D., Whitaker, K. E., Brammer, G., et al. 2010, *ApJ*, 725, 1277

Marchetti, A., Granett, B. R., Guzzo, L., et al. 2013, *MNRAS*, 428, 1424

Marigo, P. & Girardi, L. 2007, *A&A*, 469, 239

Marulli, F., Bolzonella, M., Branchini, E., et al. 2013, *ArXiv e-prints*

Mellier, F. et al. 2008, <http://terapix.iap.fr/cpl/oldSite/Descart/CFHTLS-T0005-Release.pdf>

Meneux, B., Guzzo, L., de La Torre, S., et al. 2009, *A&A*, 505, 463

Mignoli, M., Zamorani, G., Scoddeggio, M., et al. 2009, *A&A*, 493, 39

Moresco, M., Pozzetti, L., Cimatti, A., et al. 2010, *ArXiv e-prints*

Mortlock, A., Conselice, C. J., Bluck, A. F. L., et al. 2011, *MNRAS*, 413, 2845

Moster, B. P., Naab, T., & White, S. D. M. 2013, *MNRAS*, 428, 3121

Moster, B. P., Somerville, R. S., Newman, J. A., & Rix, H.-W. 2011, *ApJ*, 731, 113

Moustakas, J., Coil, A., Aird, J., et al. 2013, *ArXiv e-prints*

Mutch, S. J., Poole, G. B., & Croton, D. J. 2013, *MNRAS*, 428, 2001

Newman, J. A. & Davis, M. 2002, *ApJ*, 564, 567

Noeske, K. G., Weiner, B. J., Faber, S. M., et al. 2007, *ApJ*, 660, L43

Oke, J. B. 1974, *ApJS*, 27, 21

Pacifici, C., Kassian, S. A., Weiner, B., Charlot, S., & Gardner, J. P. 2013, *ApJ*, 762, L15

Panther, B., Heavens, A. F., & Jimenez, R. 2004, *MNRAS*, 355, 764

Peng, Y., Lilly, S. J., Kovač, K., et al. 2010, *ApJ*, 721, 193

Pérez-González, P. G., Rieke, G. H., Villar, V., et al. 2008, *ApJ*, 675, 234

Pforr, J., Maraston, C., & Tonini, C. 2012, *MNRAS*, 422, 3285

Pozzetti, L., Bolzonella, M., Lamareille, F., et al. 2007, *A&A*, 474, 443

Pozzetti, L., Bolzonella, M., Zucca, E., et al. 2010, *A&A*, 523, A13

Pozzi, F., Vignali, C., Comastri, A., et al. 2007, *A&A*, 468, 603

Prada, F., Klypin, A. A., Cuesta, A. J., Betancort-Rijo, J. E., & Primack, J. 2012, *MNRAS*, 423, 3018

Prevot, M. L., Lequeux, J., Prevot, L., Maurice, E., & Rocca-Volmerange, B. 1984, *A&A*, 132, 389

Rudnick, G., Rix, H.-W., Franx, M., et al. 2003, *ApJ*, 599, 847

Salpeter, E. E. 1955, *ApJ*, 121, 161

Santini, P., Fontana, A., Grazian, A., et al. 2012, *A&A*, 538, A33

Schechter, P. 1976, *ApJ*, 203, 297

Schmidt, M. 1968, *ApJ*, 151, 393

Scoddeggio, M., Franzetti, P., Garilli, B., Le Fèvre, O., & Guzzo, L. 2009, *The Messenger*, 135, 13

Scoddeggio, M., Franzetti, P., Garilli, B., et al. 2005, *PASP*, 117, 1284

Scrimgeour, M. I., Davis, T., Blake, C., et al. 2012, *MNRAS*, 425, 116

Somerville, R. S., Hopkins, P. F., Cox, T. J., Robertson, B. E., & Hernquist, L. 2008, *MNRAS*, 391, 481

Somerville, R. S., Lee, K., Ferguson, H. C., et al. 2004, *ApJ*, 600, L171

Springel, V., White, S. D. M., Jenkins, A., et al. 2005, *Nature*, 435, 629

Strateva, I., Ivezić, Ž., Knapp, G. R., et al. 2001, *AJ*, 122, 1861

Takeuchi, T. T., Yoshikawa, K., & Ishii, T. T. 2000, *ApJS*, 129, 1

Trenti, M. & Stiavelli, M. 2008, *ApJ*, 676, 767

Vergani, D., Scoddeggio, M., Pozzetti, L., et al. 2008, *A&A*, 487, 89

Vulcani, B., Poggianti, B. M., Aragón-Salamanca, A., et al. 2011, *MNRAS*, 412, 246

Vulcani, B., Poggianti, B. M., Oemler, A., et al. 2013, *A&A*, 550, A58

Wang, L., De Lucia, G., & Weinmann, S. M. 2013, *MNRAS*, 793

Wuyts, S., Förster Schreiber, N. M., Lutz, D., et al. 2011, *ApJ*, 738, 106

Xu, C. K., Shupe, D. L., Béthermin, M., et al. 2012, *ApJ*, 760, 72

York, D. G., Adelman, J., Anderson, Jr., J. E., et al. 2000, *AJ*, 120, 1579

Zahid, H. J., Kewley, L. J., & Bresolin, F. 2011, *ApJ*, 730, 137

Zibetti, S., Gallazzi, A., Charlot, S., Pierini, D., & Pasquali, A. 2013, *MNRAS*, 428, 1479

Zucca, E., Bardelli, S., Bolzonella, M., et al. 2009, *A&A*, 508, 1217

Zucca, E., Ilbert, O., Bardelli, S., et al. 2006, *A&A*, 455, 879

¹ INAF - Osservatorio Astronomico di Bologna, via Ranzani 1, I-40127, Bologna, Italy

² Dipartimento di Fisica e Astronomia - Università di Bologna, viale Berti Pichat 6/2, I-40127 Bologna, Italy

³ Institute of Astronomy and Astrophysics, Academia Sinica, P.O. Box 23-141, Taipei 10617, Taiwan

⁴ Aix Marseille Université, CNRS, LAM (Laboratoire d'Astrophysique de Marseille) UMR 7326, 13388, Marseille, France

⁵ Canada-France-Hawaii Telescope, 65–1238 Mamalahoa Highway, Kamuela, HI 96743, USA

⁶ SUPA, Institute for Astronomy, University of Edinburgh, Royal Observatory, Blackford Hill, Edinburgh EH9 3HJ, UK

⁷ INAF - Istituto di Astrofisica Spaziale e Fisica Cosmica Milano, via Bassini 15, 20133 Milano, Italy

⁸ INAF - Osservatorio Astronomico di Trieste, via G. B. Tiepolo 11, 34143 Trieste, Italy

⁹ INAF - Osservatorio Astronomico di Brera, Via Brera 28, 20122 Milano, via E. Bianchi 46, 23807 Merate, Italy

¹⁰ Dipartimento di Fisica, Università di Milano-Bicocca, P.zza della Scienza 3, I-20126 Milano, Italy

¹¹ INAF - Osservatorio Astrofisico di Torino, 10025 Pino Torinese, Italy

¹² Aix-Marseille Université, CNRS, CPT (Centre de Physique Théorique) UMR 7332, F-13288 Marseille, France

¹³ Dipartimento di Matematica e Fisica, Università degli Studi Roma Tre, via della Vasca Navale 84, 00146 Roma, Italy

¹⁴ INFN, Sezione di Roma Tre, via della Vasca Navale 84, I-00146 Roma, Italy

¹⁵ INAF - Osservatorio Astronomico di Roma, via Frascati 33, I-00040 Monte Porzio Catone (RM), Italy

¹⁶ Laboratoire Lagrange, UMR7293, Université de Nice Sophia-Antipolis, CNRS, Observatoire de la Côte d'Azur, 06300 Nice, France

¹⁷ Institute of Physics, Jan Kochanowski University, ul. Świetokrzyska 15, 25-406 Kielce, Poland

¹⁸ Department of Particle and Astrophysical Science, Nagoya University, Furo-cho, Chikusa-ku, 464-8602 Nagoya, Japan

¹⁹ INFN, Sezione di Bologna, viale Berti Pichat 6/2, I-40127 Bologna, Italy

²⁰ Institute d'Astrophysique de Paris, UMR7095 CNRS, Université Pierre et Marie Curie, 98 bis Boulevard Arago, 75014 Paris, France

²¹ Astronomical Observatory of the Jagiellonian University, Orla 171, 30-001 Cracow, Poland

²² National Centre for Nuclear Research, ul. Hoza 69, 00-681 Warszawa, Poland

²³ Universitätssternwarte München, Ludwig-Maximilians Universität, Scheinerstr. 1, D-81679 München, Germany

²⁴ Max-Planck-Institut für Extraterrestrische Physik, D-84571 Garching b. München, Germany

²⁵ Institute of Cosmology and Gravitation, Dennis Sciama Building, University of Portsmouth, Burnaby Road, Portsmouth, PO1 3FX

²⁶ INAF - Istituto di Astrofisica Spaziale e Fisica Cosmica Bologna, via Gobetti 101, I-40129 Bologna, Italy

²⁷ INAF - Istituto di Radioastronomia, via Gobetti 101, I-40129, Bologna, Italy

²⁸ Università degli Studi di Milano, via G. Celoria 16, 20130 Milano, Italy

²⁹ Institut Universitaire de France, 103, bd. Saint-Michel, F-75005 Paris, France